EXPERIMENTAL AND NUMERICAL ANALYSIS OF HEAT TRANSFER IN A PARTICLE-BASED CONCENTRATED SOLAR POWER RECEIVER

by

Tyler C. Ketchem

A thesis submitted to the Faculty and the Board of Trustees of the Colorado School of Mines in partial fulfillment of the requirements for the degree of Master of Science (Mechanical Engineering).

Golden, Colorado

Date ________________________

Signed: ________________________
Tyler C. Ketchem

Signed: ________________________
Dr. Greg Jackson
Thesis Advisor

Signed: ________________________
Dr. Robert Braun
Thesis Advisor

Golden, Colorado

Date ________________________

Signed: ________________________
Dr. Greg Jackson
Professor and Head
Department of Mechanical Engineering

ABSTRACT

A new concept has been developed by the National Renewable Energy Laboratory to realize the advantages of particle-based concentrated solar power with thermal energy storage. This concept uses an array of horizontal, hexagonal absorber tubes to capture sunlight and transfer heat to particles flowing over the heated tube surfaces. The granular flow heat transfer characteristics are critical to the design of the system but are not well understood. This research seeks to characterize heat transfer within this solar receiver concept by experimentally measuring heat transfer coefficients and developing a model capable of simulating a full-scale receiver by utilizing existing heat transfer correlations.

Experiments conducted on a small-scale tube array showed the dynamic nature of the particle flow and the dependence of the heat transfer coefficients on particle contact. The top tube face has particle contact along its full length, the side face has intermittent contact and the bottom face has little to none. The top face heat transfer coefficient was found to be roughly 320 W/m^2-K, over ten times greater than the bottom face, while the average heat transfer coefficient for a single tube was roughly 175 W/m^2-K using 300 µm particles.

A numerical model was then developed that includes both the solar and particle sides of the absorber tubes. Three-dimensional view factor relations capture incoming flux and reradiation effects while a unique heat transfer correlation from the literature was used for each face. The top face was treated as an inclined plate, the side face as a smooth-walled vertical channel, and the bottom face by considering heat transfer in a thin channel of the pure gas phase. Relevant flow parameters for these correlations were obtained through a one-dimensional model of the particle flow dynamics. Simulation of the full-scale receiver at intended operating conditions shows significant improvement in the convective and effective heat transfer coefficients due to increased bulk conductivity and thermal diffusivity of the granular flow at high temperatures and greatly increased contributions from radiation.

TABLE OF CONTENTS

LIST OF FIGURES

LIST OF TABLES

LIST OF SYMBOLS

Modified Froude number	Fr^*
Average Nusselt number defined by hydraulic diameter	$\overline{Nu_{\mathrm{D}}}$
Average Nusselt number defined by particle diameter	$\overline{Nu_{\mathrm{d}}^*}$
Local Nusselt number	Nu_x
Modified Peclet number	Pe_{L}^*
Prandtl number	Pr
Reynolds number	Re
Tube surface area	A_{t}
Particle phase specific heat	c_{p}
Particle flow depth	d
Hydraulic diameter	D_{h}
Length of node in particle flow direction	dx
Average particle diameter	d_{p}
Inner tube surface emissivity	e_{in}
Particle material emissivity	e_{p}
Particle curtain emissivity	e_{c}
Tube particle side emissivity	e_{t}
Radiation view factor	$F_{i,j}$
Gravitationl constant	g
Channel height	H

Average convective heat transfer coefficient . . . $\overline{h}$

Convective heat transfer coefficient . . . h_{conv}

Effective heat transfer coefficient . . . h_{eff}

Bulk conductivity of particle phase . . . k

Gas phase conductivity . . . k_g

Solids material conductivity . . . k_s

Tube wall conductivity . . . k_{t}

Plate length . . . L

Tube length . . . L_{t}

Particle mass flow rate . . . $\dot{m}$

Nodes per tube face . . . N_{face}

Volumetric energy input . . . $\dot{q}$

Heater power . . . q_{h}

Incoming solar flux . . . q''_{solar}

Cold reservoir temperature . . . T_{C}

Gas temperature . . . T_{g}

Mean gas temperature . . . $\overline{T_{\text{g}}}$

Hot reservoir temperature . . . T_{H}

Tube wall temprature . . . T_{t}

Particle temperature . . . T_{p}

Wall temperature adjacent to particle flow . . . T_{W}

Air channel height/thickness . . . t

Tube wall thickness . . . t_{t}

Average particle flow velocity v

Average gas velocitty . . . . v_{g}

Channel width . . . . W

"Effective" film thickness . . . . x_{eff}

Dimensionless entry length . . . . x^*

Particle curtain thickness . . . . z_{c}

Particle phase thermal diffusivity . . . . $\alpha = \frac{k}{\rho c_{\mathrm{p}}}$

Heat transfer empirical constant . . . . β

Ergun particle drag coefficient . . . . β_{v}

Gas volume fraction within the particle flow . . . . γ

Bed friction coefficient . . . . δ

Temperature residual criteria . . . . ΔT_{res}

Solids volume fraction within flow depth . . . . ϵ

Critical solids volume fraction . . . . ϵ_{c}

Carnot efficiency . . . . η_{Carnot}

Plate inclination angle . . . . θ

Gas viscosity . . . . μ_{g}

Bulk particle phase density . . . . $\rho = \epsilon\rho_{\mathrm{s}}$

Gas density . . . . ρ_{g}

Solids material density . . . . ρ_{s}

Stephen-Boltzmann constant . . . . σ

Particle curtain transmissivity . . . . τ_{c}

LIST OF ABBREVIATIONS

ACKNOWLEDGMENTS

I would foremost like to thank my advisors, Dr. Greg Jackson and Dr. Robert Braun, for their assistance on this project. I would also like to thank Dr. Zhiwen Ma for allowing me to include the details of his Near-Blackbody solar receiver concept and Dr. Janna Martinek for her assistance in developing models for data analysis and advice in modeling. Additionally, I would like to thank the rest of the Concentrated Solar Power research group at the National Renewable Energy Laboratory for their assistance with the granular flow heat transfer experiments with a special thanks to Dr. Greg Glatzmaier for his efforts on the heater control system. Lastly, I would like to thank my fellow graduate students for all of their help and support.

CHAPTER 1
INTRODUCTION

Each day, more energy reaches the earth from the sun than is used by mankind in an entire year [1]. Harvesting even a small fraction of this energy has the potential to meet a large portion of the world's growing energy demand with clean renewable energy. This abundant solar energy can be captured through both photovoltaics (PV) and concentrated solar power (CSP) technologies. Although PV panels can be installed almost anywhere and are ever increasing in efficiency, CSP utilizing a central receiver tower holds great promise to deliver cost-effective, dispatchable utility-scale electricity [2]. This is in large part due to its ability to generate power on the MW scale while incorporating thermal energy storage (TES).

1.1 Concentrated Solar Power Towers

Concentrated solar power systems operate by using mirrors, or heliostats, to focus the sun's energy onto a central location to warm a heat transfer fluid. The hot fluid can then be sent through a power cycle to produce electricity or transfer its energy to a separate working fluid that runs a power cycle. In the case of a single fluid system, water is typically used as the heat transfer fluid and converted directly to steam within the solar receiver. Ongoing research seeks to directly heat gases, such as CO_2, to power high temperature Brayton cycles [3]. For two-fluid systems, oils are used as the heat transfer fluid and steam as the working fluid. These configurations only allow for power production during periods of high solar irradiance and can have significant intermittency. Incorporating TES can overcome this intermittency problem and add value to the plant by allowing for load following and overnight electricity production [4].

Thermal energy can be stored as purely sensible heat, latent heat or as thermochemical energy and can be achieved in two configurations, direct or indirect. In an indirect system, the energy of the heat transfer fluid is transferred to an energy storage medium. Alternatives considered for use as the storage medium include liquids, solid slabs of concrete and packed beds of inert solids, thermochemically reacting solids or phase change materials [5–7]. Alternatively, a direct system utilizes the heat transfer fluid as the thermal storage medium. In both configurations, energy from the storage medium is transferred to a working fluid to run a power cycle when desired.

Current state of the art TES systems use molten nitrate salts as both the heat transfer fluid and thermal storage medium in a direct configuration as shown in [5]. The salts are pumped through the receiver between hot and cold storage tanks. Electricity is generated by transferring energy from the salts to create steam and power a Rankine cycle. The use of these exotic materials, as well as the equipment needed to move these fluids, create significant costs. Additionally, the operating temperatures of these plants are limited by the temperature limitations of the salts [8]. Freezing issues are encountered at 220°C and corrosion and chemical break down occur above 650°C [9]. These temperature constraints present a significant barrier to performance. As CSP plants operate using thermodynamic power cycles, their efficiency is governed by thermodynamic principles and limited by the Carnot efficiency:

$$\eta_{Carnot} = 1 - \frac{T_{\mathrm{C}}}{T_{\mathrm{H}}} \tag{1.1}$$

where T_{H} is the temperature of the hot reservoir and T_{C} is the temperature of the cold reservoir, which is the ambient air temperature in this case. Increased efficiency, and therefore improved cost, can be achieved by increasing the upper temperature limits. Unfortunately, as discussed, current systems already operate at the upper limits of molten salts. A change in heat transfer fluids is therefore needed.

1.2 Particle-Based CSP

In the 1980's it was proposed that solid particles could be utilized as the heat transfer medium in CSP plants [10–13]. Utilizing solid particles offers several advantages over nitrate salts for CSP systems. The primary benefit is the potential for higher operating temperatures. When particles such as sand are utilized, heat transfer fluid temperatures can feasibly exceed 1000°C, greatly boosting power cycle efficiency [12, 14]. Operating temperatures are instead limited by the temperature limitations of structural components and efficiency is limited by the increasing reradiation losses from high temperature surfaces.

Like molten salts, particles can serve as both the thermal storage medium and the heat transfer fluid in a direct configuration. While stored in a packed bed silo, the granular nature of solid particles offers the unique advantage of self-insulation [9]. A temperature gradient forms across a layer of particles near the wall that acts as insulation and limits further heat loss. Energy can still be effectively transferred from the hot particles to a working fluid through the use of a fluidized bed. Additionally, the use of solid particles, such as sand, offers significant cost benefits as they are low-cost materials in comparison to molten salts.

The primary design challenge in particle-based systems is the heating of the particles as they cannot simply be pumped through irradiated tubing like a liquid. Many design configurations have been proposed [15, 16], with the most widely studied option being the falling curtain receiver [14, 17]. This design directly irradiates the particles by dropping them in a steady stream through the path of concentrated sunlight. A significant drawback of this configuration is the low residence time of the particles in the irradiated zone caused by high velocities during free fall. This leads to low particle outlet temperatures. As the particles fall, considerable thinning of the particle curtain also occurs which leads to a large portion of the sun's energy directly heating the back wall of the enclosure instead of the particles. The high temperature of the wall can lead to significant reradiation losses and structural damage [14].

1.3 Near-Blackbody Enclosed Particle Receiver Concept

A new concept developed by the National Renewable Energy Laboratory (NREL) seeks to overcome the shortcomings of existing particle-based receiver designs. This design, as shown in Figure 1.1, utilizes an array of hollow, hexagonal tubes to capture the solar energy directed by the heliostat field [18, 19]. Sunlight enters the tubes where it is spread along the length of the tube by internal reflection and reradiation. This shape seeks to emulate a blackbody by focusing the majority of reradiation from the tube walls onto adjacent tube walls. Reradiation losses to the environment are therefore greatly reduced. Particles are heated by contact with the hot tube surfaces as they cascade through the channels between the backsides of the absorber tubes. A flair on the front of each tube connects the tubes together while maintaining space between them for particle flow. A full-sized receiver will consist of hundreds of rows of absorber tubes designed for particle outlet temperatures of 800°C or higher.

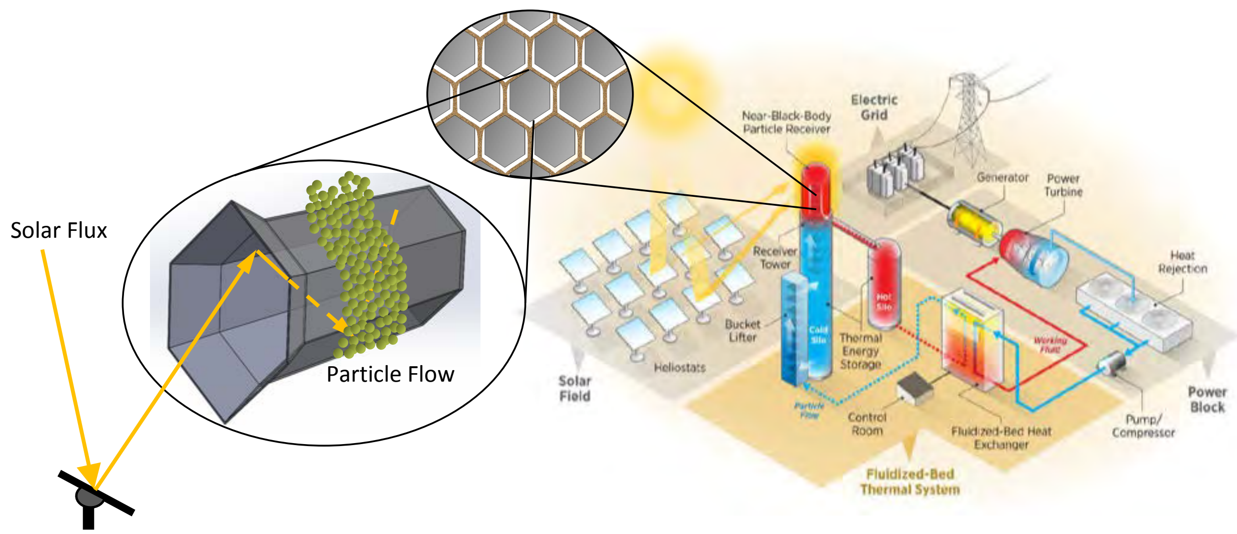

Figure 1.1: Near-Blackbody particle receiver design diagram (figure in part from [18])

1.4 Heat Transfer Considerations

An important component of the design of the NBB system is the heat transfer between the absorber tubes and the particle flow. This heat transfer largely determines the temperature of the absorber tubes for a given solar flux condition. Maximum tube temperatures drive material selection, which significantly impacts cost. Excessive temperatures could exceed the thermal limits of even the highest rated materials. Additionally, high tube temperatures lead to increased reradiation losses and decrease overall system performance. It is therefore imperative to thoroughly understand the heat transfer characteristics within the granular flow to properly design the system.

Unfortunately, heat transfer in a cascading granular flow, such as this, is complex and not well understood. A considerable number of granular flow heat transfer studies have been performed in the literature [20–35], but no correlations exist that can directly predict heat transfer in this configuration with reasonable confidence. A great deal of modeling has also been undertaken to study heat transfer in particle-based CSP systems [13, 14, 16, 18]. This literature largely focuses on falling curtain receivers that exhibit very different flow conditions than those seen in the NBB design. These models use a variety of solar radiation models and typically utilize full Lagrangian particle tracking in conjunction with fluid dynamics modeling.

Efforts by NREL to model the cascading flow seen in the NBB design have provided limited insight due to the challenges of the complex, multiphase heat transfer under consideration [18]. The model developed focuses on a single tube within the receiver array and utilizes the two-fluid model available in ANSYS Fluent. Results show heat transfer coefficients for the upper tube surface exceeding 1000 W/m^2-K and almost negligibly small for the side and bottom surfaces. The average heat transfer coefficient predicted for a single tube, therefore, is considerably lower than those observed in previous small-scale experiments [18]. This is in large part due to the perfect symmetry observed in the Fluent results that does not match the more chaotic patterns and increased particle-wall contact observed in the experiments. More complex models incorporating Lagrangian particle tracking, such as those used for falling curtain designs, could prove more effective, but are too computationally intensive for a full NBB system simulation and are not typically applicable for flows with volume fractions exceeding 10% [14, 18]. It is therefore necessary to find alternative ways to model the system and to directly measure the heat transfer coefficients more thoroughly for a more comprehensive comparison.

1.5 Research Objectives

This research seeks to characterize and simulate heat transfer between the heated absorber tubes and the cascading granular flow to support and inform effective NBB receiver design. This heat transfer is greatly impacted by the nature of the granular flow and is not well understood. Specifically, this research aims to:

- Experimentally determine an average heat transfer coefficient for each face of the hexagonal absorber tubes
- Develop a numerical model for heat transfer within the NBB design capable of predicting the experimental results by utilizing existing literature correlations
- Use the model to predict heat transfer coefficients outside the range of experiments and simulate a full-sized NBB solar receiver at intended operating conditions

These objectives are addressed by first examining the relevant literature in Chapter 2. Experimental measurement of the heat transfer coefficient is discussed in Chapter 3. Chapter 4 outlines the approach and equations used in modeling the NBB receiver design and includes a comparison to the experimental results. Simulation of a full-sized NBB receiver is discussed in Chapter 5 with overall conclusions given in Chapter 6.

CHAPTER 2

LITERATURE REVIEW

In order to fully characterize heat transfer within the NBB design it is important to understand the effects of all heat transfer modes. The dense granular flows within the design have well known radiation effects, therefore, it is important to focus on understanding heat transfer through convection and by direct particle contact. It is also important to understand the granular flow dynamics and their impact on heat transfer. Although no previous studies focused on granular flow in a configuration exactly like the NBB design, there is an abundance of existing literature that can be utilized in its analysis. These include other CSP modeling efforts as well as studies examining the heat transfer and flow characteristics of granular flows in a variety of other configurations.

2.1 Heat Transfer in Granular Flows

The relevant literature pertaining to heat transfer in granular flows can be divided into fluidized beds [20–24], flows over tube bundles [25–27], flows over flat plates [28–31], flows in vertical channels [28, 32, 33] and pneumatic conveying of particles [34, 35].

2.1.1 Fluidized Beds

The work pertaining to fluidized beds is largely summarized in the work of Chen [20]. Chen argues that the many empirical correlations developed through numerical fitting of experimental data [21–23] have limited use as their applicability only covers the narrow range of operating conditions used in their development. Instead, the use of a mechanistic model is advocated. The most widely accepted model stems from the work of Mickley and Fairbanks [24]. This model is developed by considering discrete packets of particles that move as a unit and persist for short time intervals. These packets circulate through the bed and periodically contact the heat transfer surfaces and transfer heat. An important finding from this work is the dependence of the heat transfer coefficient upon the square root of the conductivity of the particle phase. Chen refers to this as the surface renewal model and developed an equation to solve directly for the heat transfer coefficient in fluidized beds that better encompasses the trends found in multiple experimental settings.

2.1.2 Tube Bundles

Studies considering heat transfer between horizontal tube bundles and granular material focus on circular tubes and include fluidized bed [23] (discussed above), plug flow [25–27] and trickling flow [36] applications. In plug flow the particles move more slowly than in free fall conditions and are found to maintain contact with the tubes except for a small section of flow separation at the bottom of each tube. Particles also collect on the upper tube surface and form a pyramid shaped wedge of stagnant particles. The exact shape and size of the stagnation zone depends upon the arrangement of the tubes and not the flow velocity [25]. Heat transfer is found to be minimal in the stagnation zone above the tube as well as in the void zone below the tube and instead primarily occurs along the sides of the tube. Increasing the mass flow rate improves overall heat transfer [26].

For trickling granular flow over a staggered bank of horizontal tubes, the particles are again seen to collect and form a stagnation zone on the upper surface. The entire bottom half of the tube has virtually no contact due to separation from the surface in free fall conditions. The heat transfer coefficient for the upper surface is, therefore, much greater than for the lower surface. The peak heat transfer coefficient occurs at the stagnation point for low mass flow rates but moves along the perimeter towards a point at an angle of 45° from the vertical as mass flow rates increase. This is due to increased accumulation of particles with increasing mass flow rates that inhibit heat transfer at the stagnation point. Increasing the mass flow rate leads to an overall increase in heat transfer, however. It was also found that decreasing both the tube diameter and the particle size improve heat transfer [36].

2.1.3 Flat Plates

A simple configuration that has been relatively widely studied is that of the flat plate. There are two fundamental ways to examine such a granular flow. The first is by considering it to be a collection of discrete particles and the second is to assume a continuum, more similar to a conventional fluid. By developing equations governing each situation and comparing these to experimental data, Sullivan and Sabersky [28] found that a combination of these approaches is most appropriate. Their preferred model treats granular flow as a continuum with a thermal resistance at the contact surface. This is because the granular nature of the particles allows for adequate particle to particle contact but results in poor contact at the heat transfer surface. Thermal resistance is modeled as pure conduction through a thin layer of the interstitial gas phase. The thickness of this layer is referred to as the "effective" film thickness. Experimental results of plug flow down a heated, vertical chute showed an "effective" film thickness of 1/10 the diameter of a single particle. The resulting correlation is dependent upon the "effective" film thickness as well as a modified Peclet number.

This concept was expanded to inclined channels and analyzed over a wider range of Peclet numbers by the work of Spelt, Brennan and Sabersky [29]. It was discovered that the heat transfer coefficient increased with increasing velocity, as expected, but only to a certain point, after which the heat transfer decreased with continued increases in velocity. The values at high Peclet numbers therefore deviated from those predicted by the Sullivan and Sabersky correlation. This was believed to be due to changes in the density near the heated surface. It was also discovered that the heat transfer coefficient was dependent upon the depth of the flow, a parameter not previously encountered. The work of Patton et al [30] developed an updated heat transfer correlation to capture these effects by measuring the bulk flow density for each test. This led to the inclusion of a modified Froude number and a correlation for heat transfer dependent upon the inclination angle and flow depth. The applicability of this heat transfer correlation was validated through experiments by Golob [31].

2.1.4 Vertical Channels

Granular flow through a vertical channel was considered by Sullivan and Sabersky in developing the "effective" film thickness concept [28]. The experiments considered plug flow through a vertical channel with smooth walls. This work was further expanded by the work of Natarajan and Hunt [32, 33]. They showed that heat transfer in sheared flows in vertical channels, simulated by using rough walls, did not follow the equation developed by Sullivan and Sabersky beyond low Peclet numbers. Heat transfer in these cases was considerably lower and showed a peak Nusselt number at a critical Peclet number before decreasing. This decrease is not seen in plug flows. A model based on the kinetic theory of gases was developed that more accurately predicts heat transfer for shear flows. A simple correlation like those for flat plates was not developed.

2.1.5 Pneumatic Transport of Particles

An additional case studied is that of heat transfer during pneumatic conveying of particles [34, 35]. This is a case often encountered in industrial applications. Studies focus on low particle volume fractions and mostly depend upon convection through the flowing gas. It was also determined that increases in particle volume fractions improve heat transfer up to a certain point before a critical value is reached. Further addition of particles impedes their ability to adequately mix and decreases heat transfer.

2.2 Granular Flow Dynamics

While the Navier-Stokes equations can be used to describe fluid flow, there are currently no constitutive equations capable of completely describing granular flow [37]. Granular flows are instead characterized by three different regimes. These are a "dense quasi-static" regime, a "gaseous" regime and a "liquid" regime between the two [37]. The liquid regime is most similar to the dense granular flow under consideration. In such a flow, the particles largely maintain contact with one another and both collision and friction interactions play a significant roll. Such flows are widely studied in a variety of configurations as discussed in both [37] and [38]. The primary configuration applicable to this research is the flat plate.

Granular flows down flat plates can be divided into dilute or dense flows over either flat, frictional bases or "bumpy" bases [39]. For dense flows over flat bases, a shear layer develops near the surface which supports a plug flow above. Nearly constant volume fractions and velocities are observed through the depth of the flow [39, 40]. Additionally, the volume fraction is observed to be constant along the length of the plate. This constant value is dependent upon the inclination angle and decreases for steeper inclines [38]. Modeling efforts for such flows treat the volume fraction as constant for a given inclination angle and allow the depth of the flow to decrease as the particles accelerate [41, 42]. These models also include both static and rate dependent frictional terms.

CHAPTER 3
EXPERIMENTS

Although several of the granular heat transfer correlations discussed in the literature review hold promise to predict heat transfer in the hexagonal tube arrangement, none were developed for a sufficiently similar flow geometry to give complete confidence in their predictive capabilities. It was therefore determined that direct experimental results must be obtained. This chapter discusses the equipment, methodology and techniques used in these experiments and subsequent data analysis. All experiments were conducted at the National Renewable Energy Laboratories.

3.1 Objective

The goal of these experiments was to examine the granular flow and heat transfer characteristics in the NBB receiver configuration. Through these experiments it is important to measure both the overall, average heat transfer coefficient for each tube as well as the "local" heat transfer coefficients for each face. In this way the system can be adequately understood for design considerations.

A secondary objective of these experiments was to examine the impact of tube inclination angle on flow patterns and heat transfer. Although this aspect is not presented here, it does have some impact on the testing procedures as will be discussed.

3.2 Test Setup

A test stand was custom designed and built for these experiments. It consists of an outer frame for alignment of the components, a lifter for particle dispensing and an instrumented tube array for testing as shown in Figure 3.1. Particles are dispensed from a large drum into a hopper at the top of the rig. From here, the particles flow through a perforated flow control grate, through the tube array and deposit into a collection drum. This collection drum rests on a digital scale to collect mass flow rate data. The overall flow rate is controlled by changing the flow control grate to one with different sized holes. The drum lifter is then used to swap the drums for each subsequent test run.

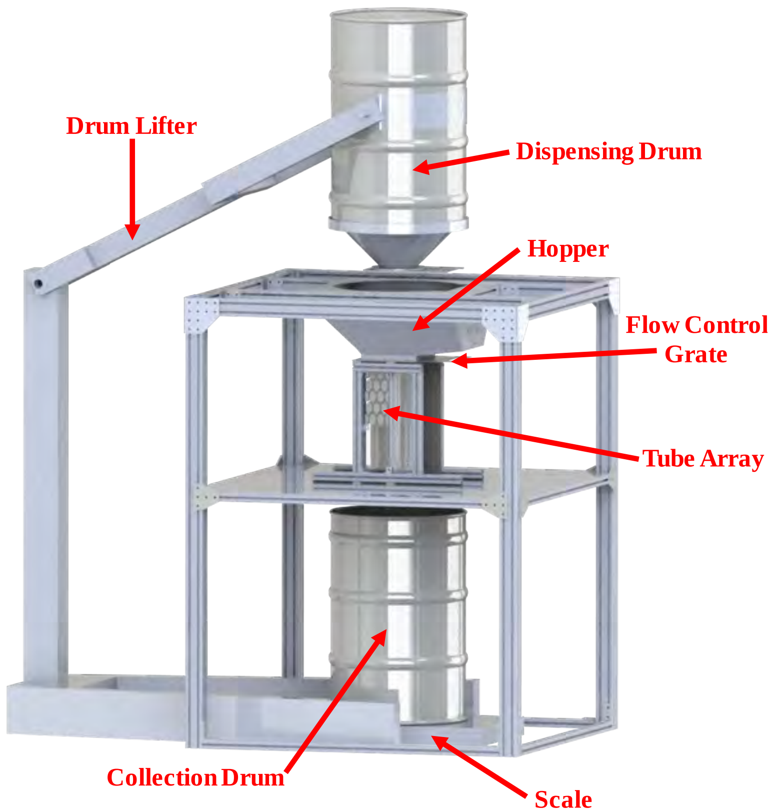

Figure 3.1: Test stand used for experiments

The tube array, see Figure 3.2(a), consists of a series of reconfigurable hexagonal tubes in an enclosure. Each tube is held in place by screws attached to the back plate. For heat transfer testing, the tubes are made of solid 6061 aluminum and identified by the row-column numbering scheme shown in Figure 3.2(b). Note that the tubes were inclined at 15° for all heat transfer testing. Mass flow distribution measurement at the outlet of the tube array showed slight changes to the mass flow rate at the ends of each tube, but flow rates near the center of the tube were scarcely affected and nearly matched the overall average mass flow rate.

Internal cartridge heaters are used to heat the middle 3 rows to simulate solar flux. The top row is unheated and serves to establish a steady state flow pattern over the heated tubes. Only partial tubes are used in the bottom row. These are again unheated and serve to maintain the proper flow pattern along the bottom face of the last row of heated tubes. Partial tubes are used for their lower heat capacity to limit heat loss from the already heated sand. Half tubes are used on the sides to maintain consistent flow.

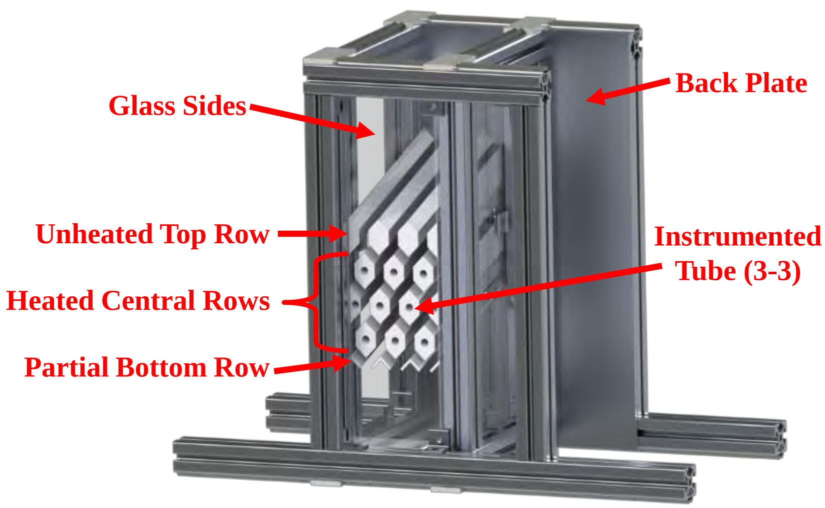

(a) Heated tube array

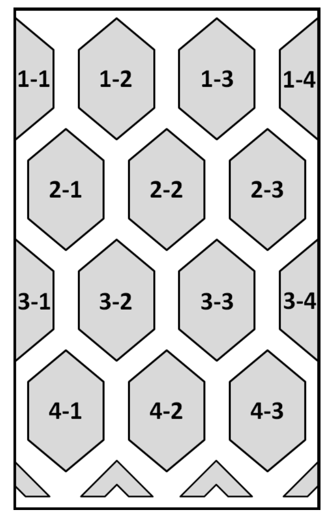

(b) Tube numbering scheme

Figure 3.2: Instrumented tube setup used for experiments

Each heated tube is configured as shown in Figure 3.3 with the dimensions shown in Figure 3.4. A cartridge heater extends the full length of the tube. The heaters are manufactured by Watlow and rated for 1 kW of power for each full tube and 500 W for each half tube. Each heater has an internal thermocouple for measuring the heater temperature and an additional thermocouple is inserted into a small hole in the tube body to measure the overall average temperature of the tube. An insulating gasket is placed between the surface of the tube and both the back plate and front glass to limit heat transfer from the ends of the tube. An additional rubber strip is placed between the insulating gasket and the front glass to hold the tube in place and prevent particles from flowing between the tube and glass. Additional insulation is placed around the outside of the tube array to limit heat losses.

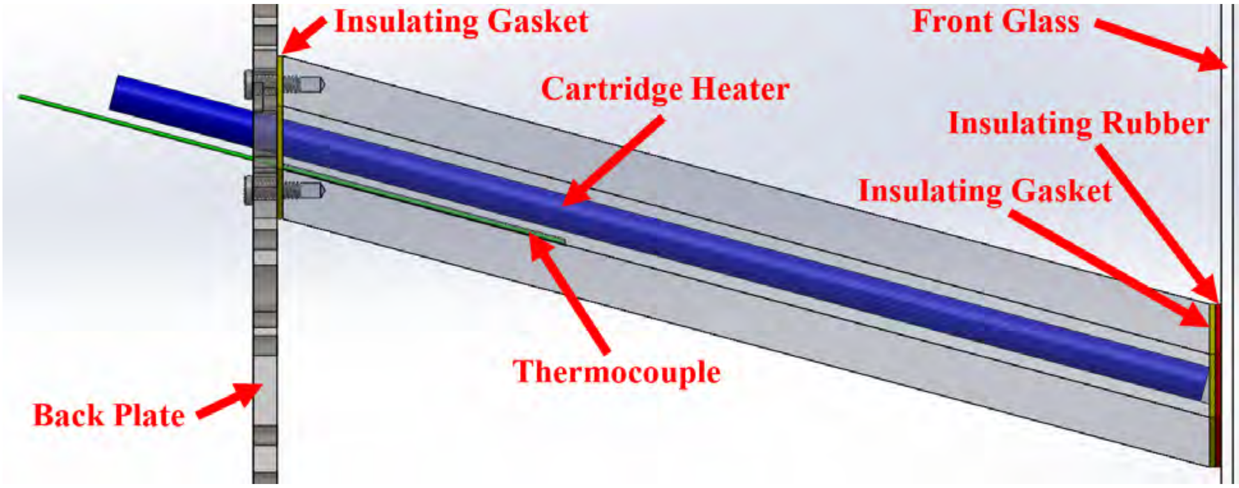

Figure 3.3: Single heated tube cross-sectional diagram

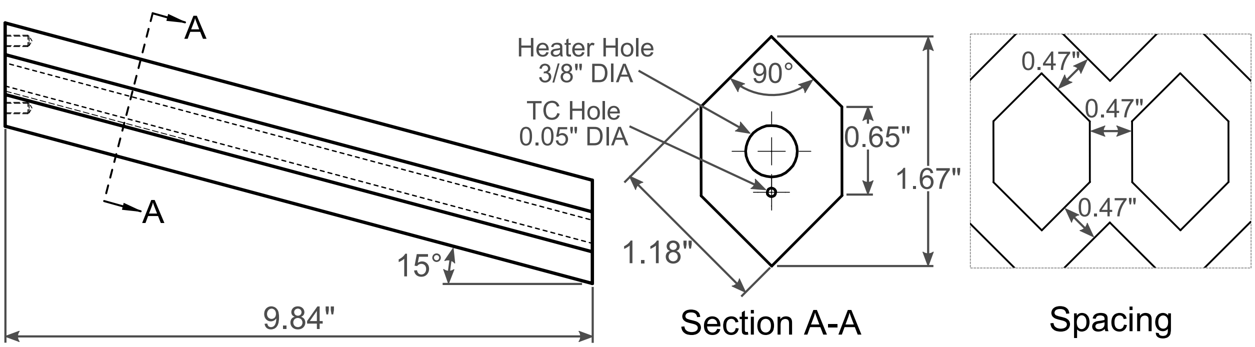

Figure 3.4: Dimensions of heated tubes used in experiments

In addition to the central thermocouple, one tube, located at position 3-3, has been outfitted with additional thermocouples for measurement of local temperatures as shown in Figure 3.5. Grooves were machined partway down the length of the tube at each vertex and along the center of each face. One thermocouple is embedded in each of these grooves and covered with thermal cement. These thermocouples serve to measure the local temperatures along the surface of the tube. A second thermocouple runs along each groove before extending into the flow to measure the local particle temperature. This is done by a gentle curve to avoid working the metal and distorting the thermocouple readings.

Thermocouples are also placed above and below the tube array to capture the inlet and outlet particle temperatures. Two inlet thermocouples are embedded within the incoming

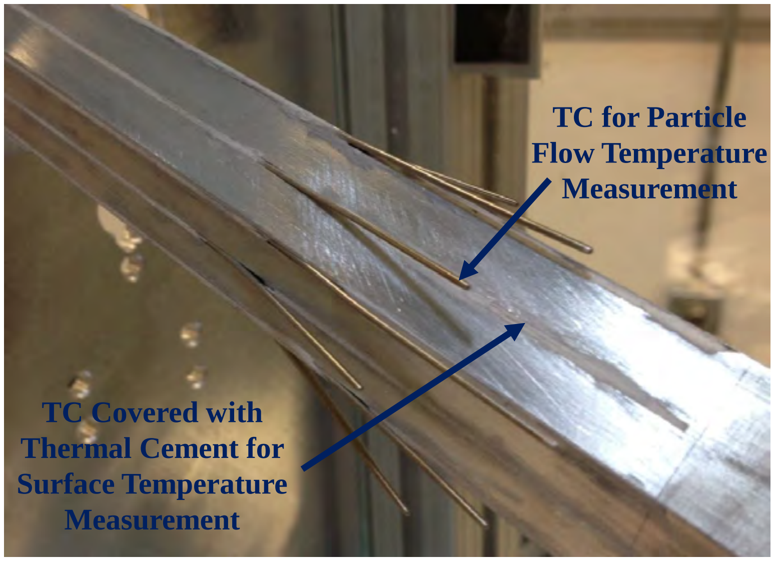

Figure 3.5: Instrumented tube for “local” heat transfer measurements

sand that collects on the flow control grate. One outlet thermocouple is placed in the center of a funneling device designed to gather and mix the outlet particles for an average reading. An additional outlet thermocouple is embedded in the particles as they collect in the collection drum. All thermocouples are sheathed, stainless-steel K-type thermocouples from Omega as detailed in Table 3.1.

Table 3.1: Specifications of thermocouples used in experiments

TC Location	Type	Diameter	Length
Tube Center	K	1/16”	6”
Instrumented Tube	K	0.040”	12”
Inlets and Outlets	K	0.040”	12”

3.2.1 Electrical Control System and Data Acquisition

The heaters are powered through the custom electrical control box shown in Figure 3.6(a). Three-phase 240 Volt electrical power is supplied to the box and runs through a contactor switch. This switch controls the flow of electricity to the box for emergency shutoff purposes. Each phase is then split and the heaters are connected evenly between each pair of phases.

Heater controllers determine the power sent to each heater individually. A power meter is connected to the leg supplying the highly instrumented tube to record its power exactly.

An additional custom data acquisition box is also used in these experiments, see Figure 3.6(b). This box is built around a cRIO data collection module from National Instruments. The thermocouples used, as well as the heater controllers, power meter and scale all connect to the cRIO which is run by a LabVIEW program driven by a desktop computer. The LabVIEW program records heater power, tube temperature and mass flow rate data. The program is also capable of controlling power to the heaters in one of two ways. In constant temperature control, a PID algorithm within the LabVIEW software maintains each heater at a constant set point by adjusting the power input. For constant power control, a constant power signal is sent to each heater controller.

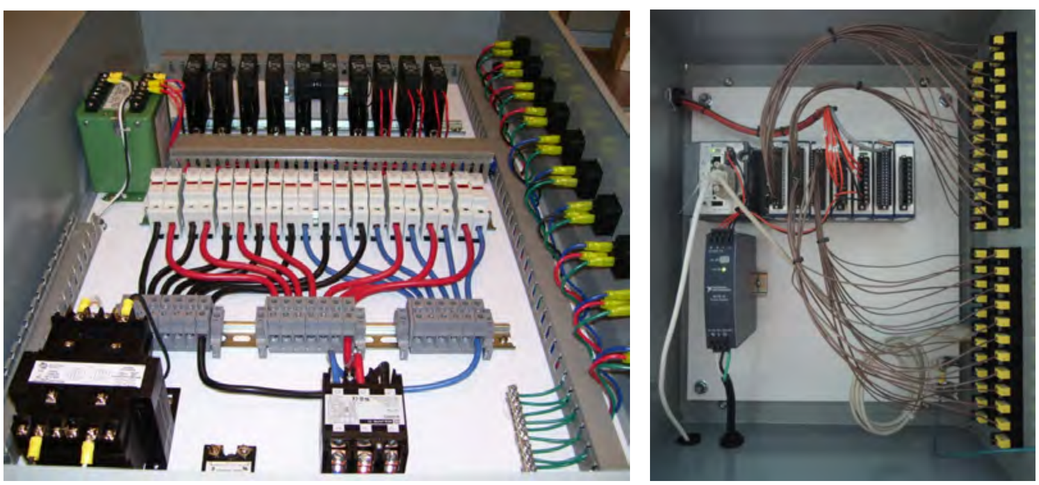

(a) Power and controls

(b) Data acquisition

Figure 3.6: Custom-built test stand electronics

3.2.2 Material Properties

The particles used for experimental testing are a clay-like substance composed of primarily silica (SiO_2) and alumina (Al_2O_3), see Table 3.2. The material properties are given in Table 3.3 where ρ_s represents the density of the solid material as determined using a mass balance and volumetric displacement. The emissivity is assumed to be that of typical sand.

Table 3.2: Composition of particles used in experiments

Compound	Composition
SiO_2	50-55%
Al_2O_3	40-45%
Fe_2O_3	0.7-1.7%
TiO_2	2.0-2.75%
K_2O	trace-1.5%
MgO	trace-0.7%
CaO	trace-0.5%
Na_2O	trace-0.5%
P_2O_5	trace-0.71%

Table 3.3: Properties of particles used in experiments

Parameter	Symbol	Value
Material density	ρ_s	2700 kg/m^3
Emissivity	e_p	0.8

Two batches of these particles were used for experiments as differentiated by their particle size distributions, see Figure 3.7. The 200 µm batch contains particles ranging from roughly 50 µm up to 400 µm centered at 200 µm. The 300 µm batch is more tightly controlled to particles ranging from approximately 150 µm up to 400 µm centered at 300 µm and is more representative of the particles expected to be used in an operational receiver.

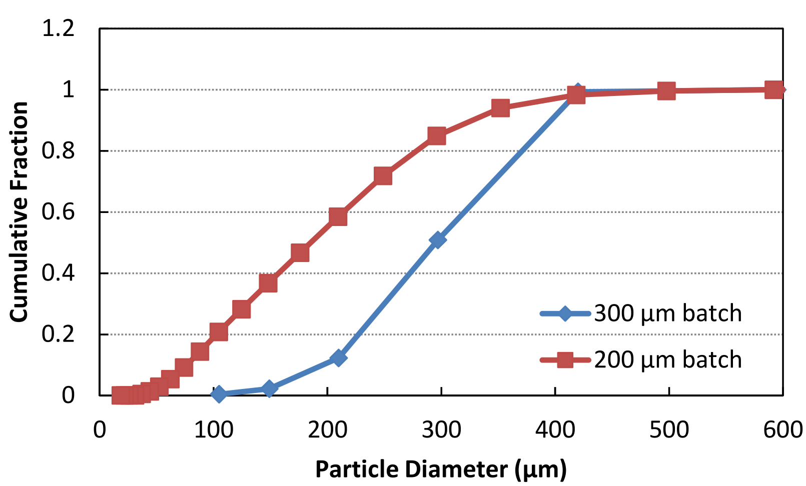

Figure 3.7: Particle batch sieve curves

3.3 Heat Transfer Testing Procedure

Heat transfer experiments were conducted by first heating the tubes to a constant temperature. Control of the tubes was then switched to constant power while particle flow was started simultaneously. This generated a first order decrease in the temperature of each tube towards a steady state value. The flow rate was sufficient to exhaust the entire 200 kg particle supply in as little as 1-2 minutes. Efforts to control for constant temperature during particle flow showed slow response times and were ineffective over the short time of experimentation. Constant power control proved much more effective as long as the starting temperature was above the steady state temperature for each tube. The tubes still did not reach steady state temperature, but the first order nature of the resulting signal allows for extrapolation to steady state values using an equation of the form

$$T_{\mathrm{t}} = C_1 e^{C_2 t} + C_3 \tag{3.1}$$

where C_1, C_2 and C_3 are constants.

3.3.1 Average Heat Transfer Data Analysis

The data was analyzed by first extracting the relevant data from the full data set. This includes the data from just after the flow starts to just before it ends. From the data it is also clear that a steady state was not reached during testing. In order to extrapolate to steady state values, the temperature data for each tube over this time frame was fit to Equation 3.1 using MATLAB.

A sample of the relevant raw data for the test duration is shown in Figure 3.8(a) and the corresponding fit data is shown in Figure 3.8(b) according to the tube numbering scheme in Figure 3.2(b). It should be noted that the wide range of steady state temperatures is typical of results. This is believed to be due to the erratic nature of the flow. Some tubes experience more particle contact than others which leads to different heat transfer characteristics for each tube.

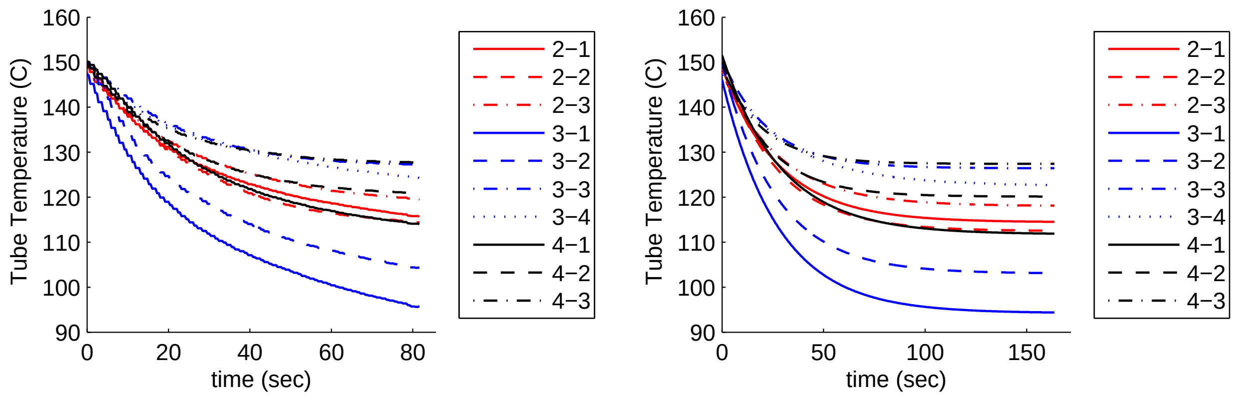

(a) Raw data

(b) Exponential fit

Figure 3.8: Sample tube temperature results

Sample data for the particle temperatures is shown in Figure 3.9(a) and for the input power in Figure 3.9(b). Note that tubes 3-1 and 3-4 are half tubes which contain smaller heaters and receive half the power of the others.

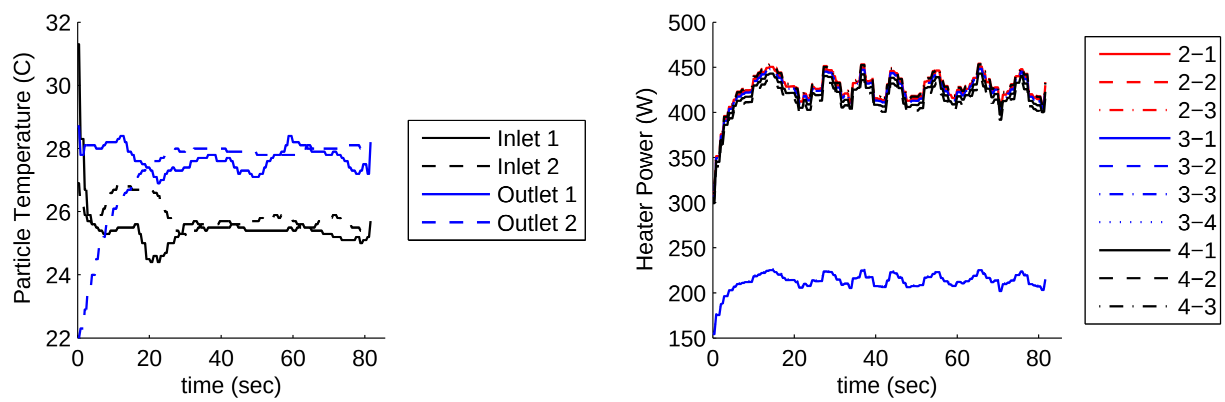

(a) Particle temperature

(b) Heater power

Figure 3.9: Sample particle temperature and power input results

Only the power supplied to tube 3-3 was explicitly measured by a power meter, the others must be inferred. To do this, the voltage applied to the heater in tube 3-3 is back calculated from the measured power, known heater resistance and the recorded heater duty cycle sent to the controller. As the heaters are connected to a single power source and in the same configuration, the applied voltage was assumed to be the same for all heaters. This was also verified through direct measurement. The calculated applied voltage was then used with the known resistance and the recorded duty cycle of each other heater to calculate the individual power inputs.

This method proved more accurate than using an energy balance between the inlet and outlet particle temperatures to determine power input as the precision of the thermocouples over a temperature increase of only a few degrees Celsius is prohibitive. The average power input to each tube was calculated by averaging the power input over the duration of the test. The average mass flow rate was calculated by taking the slope from a linear fit of the mass versus time data. The inlet and outlet particle temperatures were found by taking the average over the second half of the test duration. An average particle temperature for each row was found by dividing the change in temperature from the inlet to the outlet by the number of heated rows and assuming a linear increase by row.

Once the steady state values were determined, the average heat transfer coefficient, $\bar{h}$, for each tube was calculated by

$$\bar{h} = \frac{q_{\mathrm{h}}}{A_{\mathrm{t}}\left(T_{\mathrm{t}} - T_{\mathrm{p}}\right)} \tag{3.2}$$

where q_{h} is the heater power, T_{t} is the tube surface temperature, T_{p} is the particle flow temperature and A_{t} is the surface area of a single tube. An average heat transfer coefficient for each test run was then obtained by averaging the values for each tube.

3.3.2 "Local" Heat Transfer Coefficient Analysis

The average heat transfer coefficient (HTC) for each face was found by first extracting the steady state surface temperature results for tube 3-3 using the same exponential fit method described above. The heat transfer coefficient cannot be calculated directly as the heat flux through each face is unknown. Instead, a model was created to simulate heat transfer within the system using ANSYS Fluent. A 2D cross section of the solid tube geometry was constructed and is shown with the boundary conditions applied in Figure 3.10.

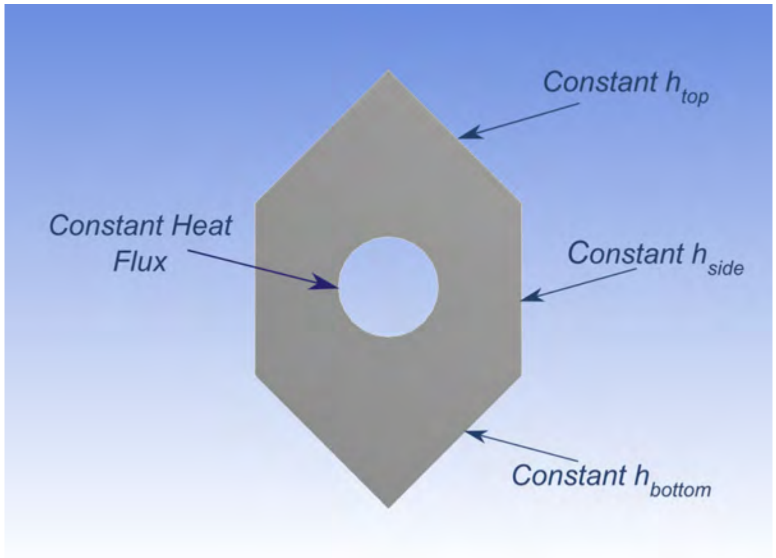

Figure 3.10: Fluent setup and boundary conditions for "local" heat transfer coefficients

The heat transfer was assumed to be a constant value across each face. A User-Defined Function (UDF) was created to update the average heat transfer coefficient for each face until the center temperature for each face matched the experimental results. Face temperatures input into the UDF were obtained by averaging the experimental results between the two sides of the tube to maintain symmetry. The heat flux boundary was set by dividing the total heater power by the surface area of the heater bore hole. The ambient temperature was set using the average particle temperature for the tube row instead of the temperatures measured by the thermocouples protruding into the flow due to inconsistencies in the data collected. For some surfaces, it was unknown if the thermocouples were even measuring the particle temperature or were instead measuring the air temperature as the exact location of the thermocouple tip could not be observed during testing. A sample of the Fluent results compared to the experimental data is shown in Figure 3.11 where the three data points at the center faces used as the input values to Fluent are indicated. The results match very well except for the two endpoints which correspond to the top and bottom vertexes of the hexagonal tube.

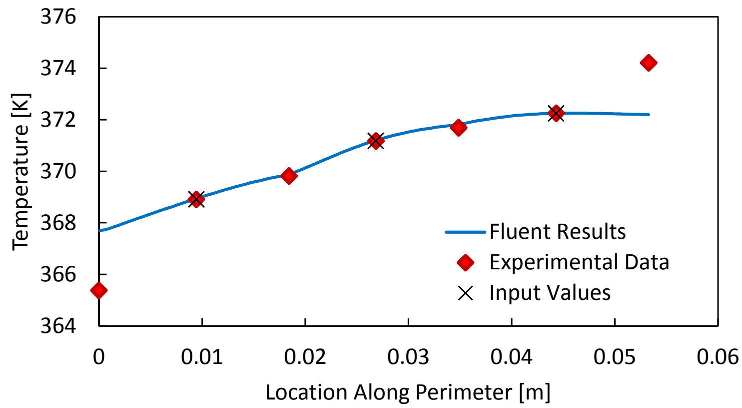

Figure 3.11: A sample of Fluent temperature results along the side of a single tube from top to bottom vertexes compared to experimental data

3.4 Results

The average heat transfer coefficient (HTC) results for both particle batches tested are shown in Figure 3.12 where each point represents the average of the individual h values measured for a single test. The mass flow rate has been normalized for consistency with numerical results that will be discussed in Chapter 4. It can be seen that the heat transfer coefficient is improved with increasing mass flow rates, as well as slightly improved by increased heater power for a given mass flow rate. The 200 µm particle batch displays a significantly higher HTC for a given mass flow rate. The highest mass flow rate shown for each particle batch represents the highest achievable flow rate through the constructed geometry. Lower flow rates are achieved through the use of rate limiting flow control grates and higher values can not be achieved without changing the tube spacing.

The "local" heat transfer coefficient results for each face for the 300 µm particle batch are shown in Figure 3.13 and for the 200 µm batch in Figure 3.14. For the 300 µm batch, the top tube surface shows a considerably higher average HTC than the other faces except for at the lowest flow rate tested where it matches the side face value. The bottom surface exhibits minimal heat transfer while the side face heat transfer coefficient is roughly half that of the top face for higher mass flow rates. Increasing the mass flow rate shows an increase in the

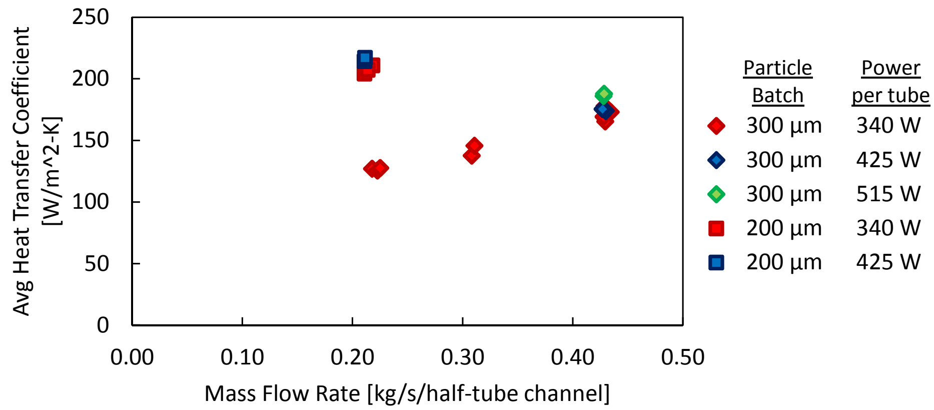

Figure 3.12: Average heat transfer coefficient results

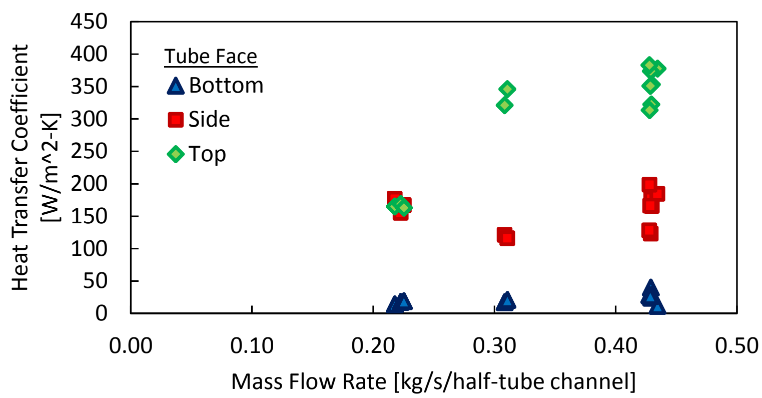

Figure 3.13: Local heat transfer coefficient results by face for the 300 µm particle batch

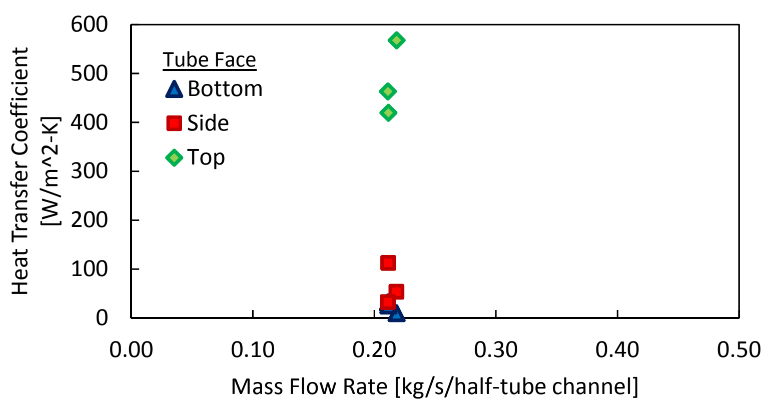

Figure 3.14: Local heat transfer coefficient results by face for the 200 µm particle batch

HTC for all faces with the exception of a dip in the side face heat transfer for moderate mass flow rates.

Results for the 200 µm particle batch show that the increase in the average heat transfer coefficient due to decreases in particle size is mostly due to increases for the top tube face. The side and bottom heat transfer coefficients show slight decreases. Results were not obtained at different flow rates.

3.4.1 Flow Visualization

Additionally, video recording of particle testing was conducted during several unheated test runs. A sample of these results at maximum flow conditions for the inclined tubes tested is shown in Figure 3.15(a). From this image we can see that there are significant differences in the flow patterns between different channels. It can also be seen that the flow over the top tube faces typically does not fill the entire channel while the vertical flow channels are packed. Some of the packing is due to the previously mentioned effect of the inclination angle on the flow at the ends of the tubes and some due to wall effects.

(a) 15° inclined tubes

(b) Horizontal tubes (image courtesy of NREL and Ohio State University)

Figure 3.15: Particle flow visualization results

Previous testing on a smaller assembly of horizontal tubes, see Figure 3.15(b), shows flow patterns more characteristic of flow at the center of the tube where the heat transfer measurements took place. Here the particle flow along the top tube surface is characterized by a significant gap between the surface of the particle flow and the under side of tube above. The depth of this flow decreases along the length of the tube face. The vertical channels are not packed as full as the inclined tube case but are still mostly filled. Flow between each channel is unique for both the vertical and inclined portions and displays significant variability.

3.5 Results Discussion

The observed increase in overall heat transfer with increasing mass flow rate is consistent with the previously reviewed literature and is largely due to the increased thermal mass of increased particle flow. Decreasing the particle diameter also increased overall heat transfer as anticipated by previous literature studies. This came at the cost of decreased mass flow, however. Lastly, increasing the heater power leads to a slight increase in heat transfer coefficients as well. This is believed to be due to a slight increase in radiation effects caused by the increased temperatures of the tube surfaces. Overall, the effects of radiation are largely negligible in the low temperature range studied and the coefficients measured represent mostly convective heat transfer.

Coupling particle flow visualization with the “local” heat transfer results shows that particle contact correlates with the heat transfer coefficients. The top face is observed to have particle contact over its entire length and a significantly higher heat transfer coefficent. The bottom face has no particle contact and a poor heat transfer coefficient while the side face is observed to have slight flow separation from the wall with intermittent particle contact and a moderate heat transfer coefficient. It is also observed that the flow in the vertical channels and the depth of the flow across the top surfaces are highly variable. This variability in flow patterns between tubes likely plays a significant role in the observed variability in the heat transfer coefficients.

CHAPTER 4

MODELING APPROACH

In order to expand the results of the heat transfer testing beyond the narrow range of operating conditions examined and for use in overall receiver design analysis, a numerical model for the NBB receiver was developed using MATLAB. This model predicts tube and particle temperatures for a full-sized receiver by incorporating both heat transfer from the heated tubes to the particles and radiative heat transfer internal to the tubes and to the surroundings. This is done through the use of simplified 1D modeling of the cascading granular flow which evaluates flow parameters relevant to heat transfer characteristics. These parameters are then used in conjunction with heat transfer correlations specific to each surface of the hexagonal tube array to calculate effective heat transfer coefficients. The simplified nature of the model allows for a full-sized receiver consisting of hundreds of rows of tubes to be simulated in a reasonable time frame while showing agreement with experimental data. This is a significant improvement over previous modeling efforts. The modeling approach and the equations used are further discussed in the following chapter.

4.1 Modeling Methodology

For analyzing the NBB receiver design, only a narrow vertical section must be examined due to symmetry in the horizontal direction. The domain is then discretized into nodes that contain tubes and those that contain flowing particles. The thin segment used for this analysis is shown in Figure 4.1 along with the repeating unit cell discretized into nodes. It is useful to distinguish between node types because they are governed by different equations. Analysis is conducted on a one-dimensional basis that neglects changes in parameters along the length of the tube. The final program operates according to the flow chart shown in Figure 4.2.

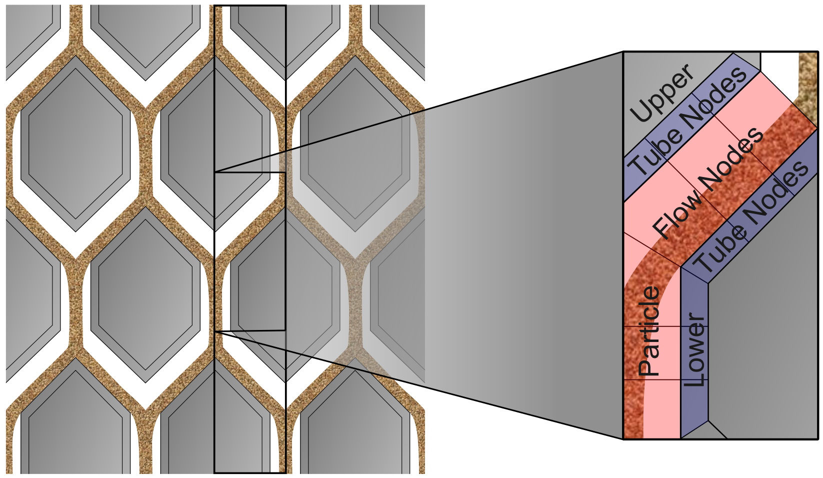

Figure 4.1: Discretized domain used for modeling

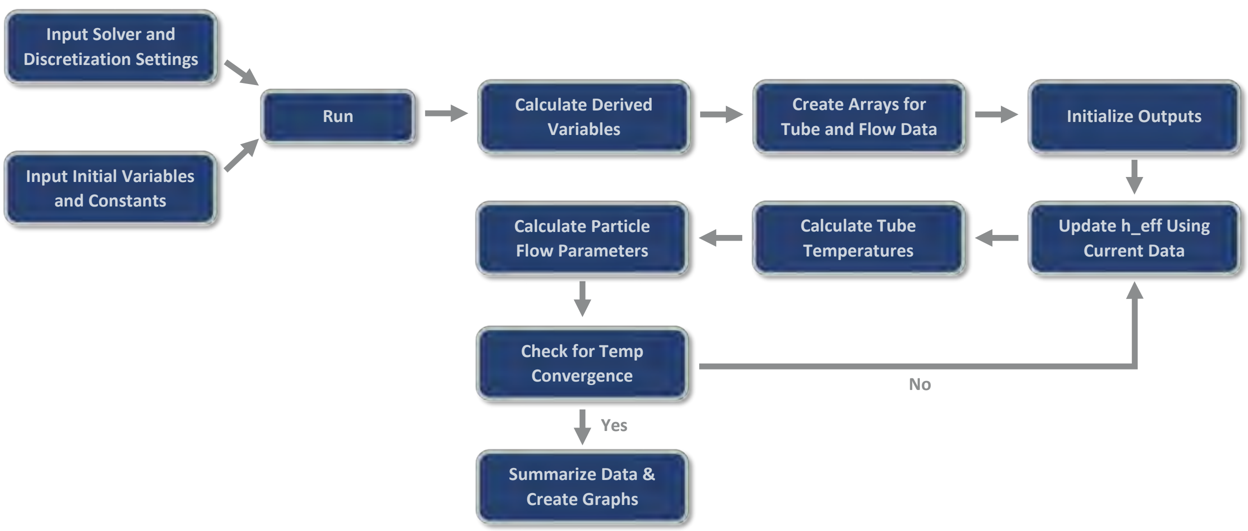

Figure 4.2: MATLAB program flow chart

The initial parameters, such as the inlet temperature and mass flow rate, can be set by the user. Once program operation commences, values for each particle flow and tube node are initialized based on these inputs. The state variable for each tube node is the tube temperature. For each particle flow node, there are five: particle temperature, particle velocity, gas velocity, solids volume fraction and particle flow depth. The gas temperature is assumed to match the particle temperature and is therefore not included as a state variable.

An effective heat transfer coefficient that includes both convection and radiation effects can then be calculated between each tube wall and the adjacent particle flow based on these state variables.

The tube temperatures are calculated using an energy balance for each node. This is done by matrix inversion assuming a constant particle temperature for each node. The particle flow state variables are then calculated by solving a mass balance on the gas flow and mass, momentum and energy balances on the particle flow. These are solved simultaneously using fsolve, one of MATLAB's built in non-linear equation solvers, and the tube temperatures and heat transfer coefficients from the previous iteration. The effective heat transfer coefficients are then updated using the new values for all nodes before the process is repeated. Iteration continues until the change in temperature of all nodes between iterations meets a desired residual criteria.

4.2 Tube Wall Equations

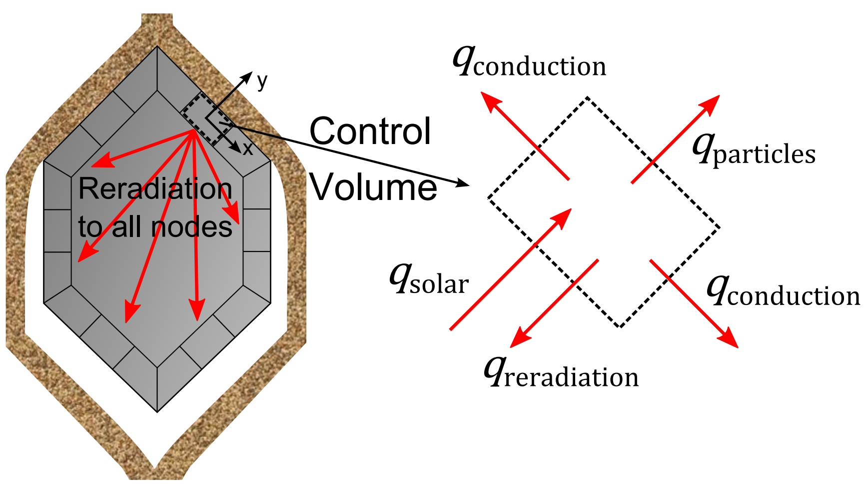

Figure 4.3: Control volume used for tube wall nodes with energy flows

The temperature of each tube node is calculated by evaluating an energy balance for each node that includes incoming solar radiation, conduction between adjacent nodes, convection and radiation to the flowing particles and reradiation inside each tube as shown in Figure 4.3

and Equation 4.1.

$$\dot{q} = -k_{\mathrm{t}} \left(\frac{\partial^2 T_{\mathrm{t}}}{\partial x^2} \right) \tag{4.1}$$

where k_{t} is the conductivity of the tube material, T_{t} is the tube wall temperature, x is the direction parallel to the tube surface and $\dot{q}$ is the net, volumetric energy input which includes incoming solar flux, outgoing reradiation and heat transfer to the particles. This equation is discretized to give

$$q''_{\mathrm{solar}} dx L_{\mathrm{t}} = t_{\mathrm{t}} L_{\mathrm{t}} \frac{k_{\mathrm{t}}}{dx} \left(2T_{\mathrm{t},i} - T_{\mathrm{t},i-1} - T_{\mathrm{t},i+1} \right) + dx L_{\mathrm{t}} h_{\mathrm{eff}} \left(T_{\mathrm{t},i} - T_{\mathrm{p}} \right) + dx L_{\mathrm{t}} q''_{\mathrm{reradiation}} \tag{4.2}$$

where t_{t} is the thickness of the tube wall, L_{t} is the length of the tube, h_{eff} is the effective heat transfer coefficient between the tube surface and particle flow and T_{p} is the particle temperature adjacent to the surface. The reradiation from a node i to all other nodes and to the ambient is found using

$$q''_{\mathrm{reradiation}} = \sum_{j=1}^{n} F_{i,j} \sigma e_{\mathrm{in}} \left(T_{\mathrm{t},i}^4 - T_{\mathrm{t},j}^4 \right) \tag{4.3}$$

where e_{in} is the emissivity of the tube's inner surface, σ is the Stefan-Boltzmann constant and the view factors, $F_{i,j}$, are found using 3-D view factor relations between nodes and by utilizing the enclosure rule for the view factor to the ambient. Although the vertical column of the NBB receiver under consideration only includes half the nodes for a given tube, radiation to the entire tube is simulated by including "phantom" nodes that are assumed to be at the same temperature as their mirrored partners. It is further assumed that the back wall of the receiver tube does not participate in radiation exchange and that heat transfer to the ambient is through reradiation only.

4.2.1 Tube Wall Conductivity

The conductivity of the tube wall is assumed to be that of stainless steel. Changes in conductivity with temperature are given by

$$k_{\mathrm{t}} = 14.6 + 0.0127 T_{\mathrm{t}} \tag{4.4}$$

where T_t is given in °C and k_t in W/m-K [43].

4.2.2 Radiation View Factors

Each hexagonal tube is discretized into long, rectangular segments which can be considered finite, three-dimensional planes. The view factor between any two of these segments can then be calculated using the proper view factor relation and geometric parameters.

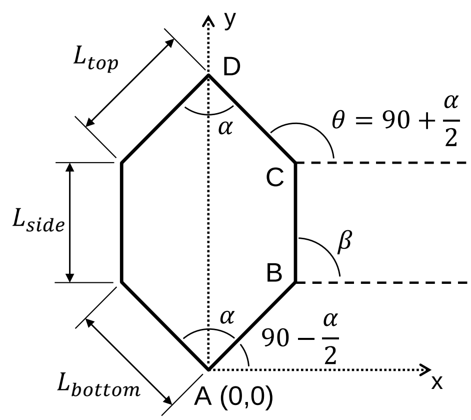

Figure 4.4: Tube input dimensions

The tube geometry is input using the dimensions shown in Figure 4.4 and the tube length. The view factor between any two arbitrary nodes is calculated by first using their coordinates to determine their relative position to one another. The appropriate view factor relation can then be selected. Lastly, the necessary geometric constraints are calculated based on the node locations and used in the proper equation.

There are three potential view factor configurations in the current hexagonal tube design, as discussed below. Although much of the modeling is performed on a 1D basis, the radiative heat transfer is calculated using view factors based on the 3D geometry of the tube and includes the dimensions shown in Figure 4.4 as well as the length of the tube. The view factor equations come from the 3rd edition of the Catalog of Radiation and Heat Transfer Configuration Factors [44].

Offset Parallel Planes

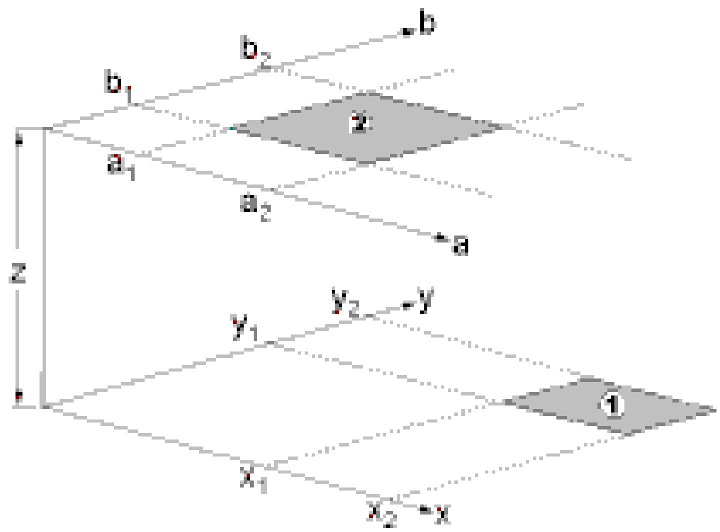

Figure 4.5: Offset parallel planes configuration

For two nodes that are on directly opposed faces, the offset parallel planes view factor relation shown in Figure 4.5 can be used. The view factor is then calculated by

$$F_{1-2} = \frac{1}{(x_2 - x_1)(y_2 - y_1)} \sum_{i=1}^{2} \sum_{j=1}^{2} \sum_{k=1}^{2} \sum_{l=1}^{2} (-1)^{i+j+k+l} G(x_i, y_j, b_k, a_l) \tag{4.5}$$

where

$$\begin{aligned} G = \frac{1}{2\pi} \Bigg[& (y-b)\sqrt{(x-a)^2 + z^2} \tan^{-1}\left(\frac{y-b}{\sqrt{(x-a)^2 + z^2}}\right) \\ & + (x-a)\sqrt{(y-b)^2 + z^2} \tan^{-1}\left(\frac{x-a}{\sqrt{(y-b)^2 + z^2}}\right) \\ & - \frac{z^2}{2} \ln\left((x-a)^2 + (y-b)^2 + z^2\right) \Bigg] \end{aligned} \tag{4.6}$$

Contacting Planes

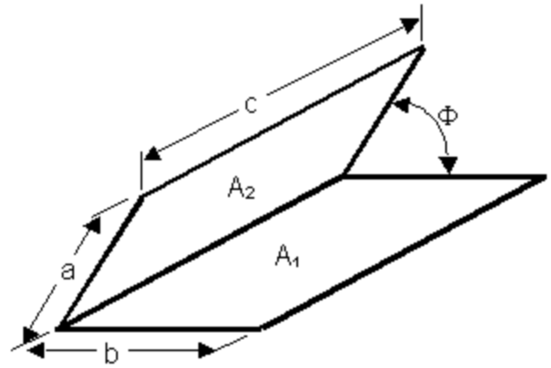

Figure 4.6: Contacting planes view factor diagram

For the case of two nodes that meet at a corner of the tube, the view factor can be determined by considering the nodes to be two contacting rectangular planes as shown in Figure 4.6. Using the dimensions shown, the view factor can be calculated by

$$\begin{aligned}
F_{1-2} = &-\frac{\sin 2\phi}{4\pi B}\left[AB\sin\phi + \left(\frac{\pi}{2}-\phi\right)\left(A^2+B^2\right) + B^2\tan^{-1}\left(\frac{A-B\cos\phi}{B\sin\phi}\right) + A^2\tan^{-1}\left(\frac{B-A\cos\phi}{A\sin\phi}\right)\right] \\
&+\frac{\sin^2\phi}{4\pi B}\left\{\left(\frac{2}{\sin^2\phi}-1\right)\ln\left[\frac{\left(1+A^2\right)\left(1+B^2\right)}{1+C}\right] + B^2\ln\left[\frac{B^2\left(1+C\right)}{\left(1+B^2\right)C}\right] + A^2\ln\left[\frac{A^2\left(1+A^2\right)^{\cos 2\phi}}{C\left(1+C\right)^{\cos 2\phi}}\right]\right\} \\
&+\frac{1}{\pi}\tan^{-1}\left(\frac{1}{B}\right) + \frac{A}{\pi B}\tan^{-1}\left(\frac{1}{A}\right) - \frac{\sqrt{C}}{\pi B}\tan^{-1}\left(\frac{1}{\sqrt{C}}\right) \\
&+\frac{\sin\phi\sin 2\phi}{2\pi B}AD\left[\tan^{-1}\left(\frac{A\cos\phi}{D}\right) + \tan^{-1}\left(\frac{B-A\cos\phi}{D}\right)\right] \\
&+\frac{\cos\phi}{\pi B}\int_0^B\sqrt{1+\zeta^2\sin^2\phi}\left[\tan^{-1}\left(\frac{\zeta\cos\phi}{\sqrt{1+\zeta^2\sin^2\phi}}\right) + \tan^{-1}\left(\frac{A-\zeta\cos\phi}{\sqrt{1+\zeta^2\sin^2\phi}}\right)\right]d\zeta
\end{aligned} \tag{4.7}$$

where

$$A = a/c \tag{4.8}$$

$$B = b/c \tag{4.9}$$

$$C = A^2 + B^2 - 2AB\cos\phi \tag{4.10}$$

$$D = \left(1 + A^2\sin^2\phi\right)^2 \tag{4.11}$$

Adjacent Planes

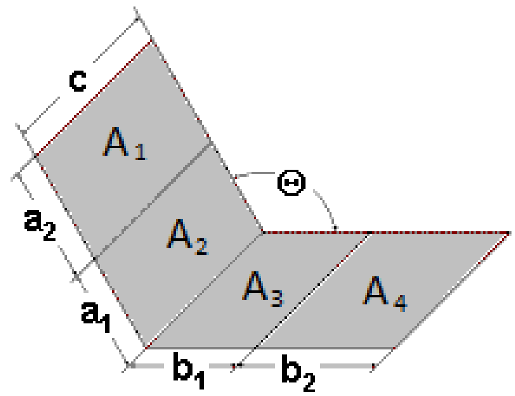

Figure 4.7: Adjacent planes diagram

The remainder of node pairs on any two arbitrary faces can be considered two nodes on adjacent, non-contacting faces as shown in Figure 4.7. The vertex where the two planes meet is not necessarily located on the tube perimeter and must be determined from the location of the nodes. The view factor between the areas of interest, A_1 to A_4, can be calculated by

$$F_{1-4} = \frac{A_1 + A_2}{A_1}(F_{12-34} - F_{12-3}) - \frac{A_2}{A_1}(F_{2-34} - F_{2-3}) \tag{4.12}$$

where F_{12-34}, for example, denotes the view factor from the entire upper plate to the entire lower plate. The intermediate steps are evaluated using the contacting planes relation in equation 4.7.

4.3 Heat Transfer Correlations

For the hexagonal geometry under consideration, no single heat transfer correlation from the literature is sufficient for predicting heat transfer from the receiver tubes to the flowing particles, especially when knowledge of the heat transfer for each face is needed. Instead, each face is treated individually. The top face is considered an angled flat plate with good particle contact, the side faces are treated as vertical plates or channels and the bottom face is treated by considering air moving through the gap between the tube surface and the air-particle interface.

4.3.1 Top Face

The most developed and useful correlation for heat transfer in gravity-driven granular flows down inclined plates comes from the work of Patton [30]. The Nusselt number for such a flow is given by

$$\overline{Nu_{\mathrm{d}}^{*}} = \frac{\overline{h}d_{\mathrm{p}}}{k_{\mathrm{g}}} = \frac{1}{x_{\mathrm{eff}} + \left(\frac{\sqrt{\pi}}{2}\right)\left(\frac{1}{\sqrt{Pe_{\mathrm{L}}^{*}}}\right)\left(1+\beta\frac{Fr^{*}}{\sqrt{Pe_{L}^{*}}}\right)} \tag{4.13}$$

where $\overline{h}$ is the average heat transfer coefficient, d_{p} is the particle diameter and k_{g} is the gas phase conductivity. x_{eff} defines the "effective" film thickness and is dependent upon the geometry of the particles and the surface. A value of $x_{\mathrm{eff}} = 0.065$ was found to apply to most smooth surfaces [30] and was used here. β is an empirical constant. A value of $\beta = 15$ is recommended [30] and was used here. The Nusselt number is also a function of Fr^{*} and Pe_{L}^{*}, which are the modified Froude and Peclet numbers, respectively. They are defined by

$$Fr^{*} = \frac{v^2}{gd\cos(\theta)}\frac{\epsilon_{\mathrm{c}}}{\epsilon}\frac{k}{k_{\mathrm{g}}}\frac{d_{\mathrm{p}}}{L} \tag{4.14}$$

$$Pe_{\mathrm{L}}^{*} = \left(\frac{k}{k_{\mathrm{g}}}\right)^2\left(\frac{d_{\mathrm{p}}}{L}\right)^2\frac{vL}{\alpha} \tag{4.15}$$

where L is the plate length, θ is the inclination angle of the plate as measured from horizontal, ϵ is the solids volume fraction of the flowing media, ϵ_{c} is the critical solids volume fraction which was taken to be 0.56 as recommended [30], k is the bulk conductivity of the particle phase, v is the average flow velocity, d is the depth of the flowing media and α is the bulk thermal diffusivity of the particle phase defined by $\alpha = \frac{k}{\rho c_{\mathrm{p}}}$ where c_{p} is the particle phase specific heat and ρ is the bulk density of the flowing media given by $\rho = \rho_s\epsilon$.

4.3.2 Side Face

Of the work pertaining to granular flows in vertical channels, the correlation of Sullivan and Sabersky [28] is most applicable to the side walls of the hexagonal geometry. This is due to the smooth walled channels used in their experiments as well as the development of a simple correlation for the Nusselt number which is given by

$$\overline{Nu_{\mathrm{d}}^{*}} = \frac{\overline{h} d_{\mathrm{p}}}{k_{\mathrm{g}}} = \frac{1}{x_{\mathrm{eff}} + \frac{\sqrt{\pi}}{2}\sqrt{\frac{1}{Pe_{\mathrm{L}}^{*}}}} \tag{4.16}$$

where the Peclet number is again given by equation 4.15 and x_{eff} again represents the "effective" film thickness. A value of $x_{\mathrm{eff}} = 0.085$ was found to give the best fit to the experimental data for vertical channels [28].

As discussed previously, this correlation was developed using data from plug flow experiments in a long vertical channel. Although similar, this differs noticeably from our flow regime where the particles are in free fall and not completely packed. Experiments also show that the particles do not maintain consistent contact with the side walls. In order to modify this correlation to fit our flow regime, the "effective" film thickness is increased to account for conduction through a larger gap between the walls and particles. The exact value used will be discussed further in Section 4.5.

4.3.3 Bottom Face

Experiments have shown that there is little to no contact between the particle flow and the bottom surface of the receiver tubes. Therefore, a heat transfer correlation was developed by considering air flow through the thin channel formed by the upper surface of the particle flow and the bottom face of the tube. The bottom tube surface is considered to be a constant flux boundary due to the solar flux incident on the solar side of the tube. The air-particle interface is treated as an insulated boundary by assuming the air and particles to be at the same temperature. The average Nusselt number for fully developed flow through a thin channel with these boundary conditions is given by [45, 46]

$$\overline{Nu_{\mathrm{D}}} = \frac{\overline{h} D_{\mathrm{h}}}{k_{\mathrm{g}}} = 5.39 \tag{4.17}$$

where $\overline{h}$ is again the average heat transfer coefficient, k_g is the gas phase conductivity and D_{h} is the hydraulic diameter of the channel given by $D_{\mathrm{h}} = \frac{4tL}{2W+2t}$ where W is the channel width and t is the channel thickness. In the case of our geometry, the channel width is defined by

$W = L_\mathrm{t}$, the length of the tube, and the air channel thickness is defined by $t = H - d$ where H is the total height of the channel and d is the depth of the particle flow.

For the short face under consideration, the flow is not fully developed, however. The dimensionless axial distance along the tube for developing flow is given by [46]

$$x^* = \frac{x}{D_\mathrm{h} Re Pr} \tag{4.18}$$

where Re and Pr are the Reynolds and Prandtl numbers for the flowing gas and x is the distance along the channel. Values of roughly $x^* < 0.25$ have significant entry length effects. Tabular values for the local Nusselt number, Nu_x, have been found for fluid flow between parallel plates with one at constant flux and the other insulated for various x^* and Pr values [46]. An equation was developed for the range of $0.001 < x^* < 0.025$ and $0.01 < Pr < 10$ by curve fitting the tabular data as shown in Figure 4.8.

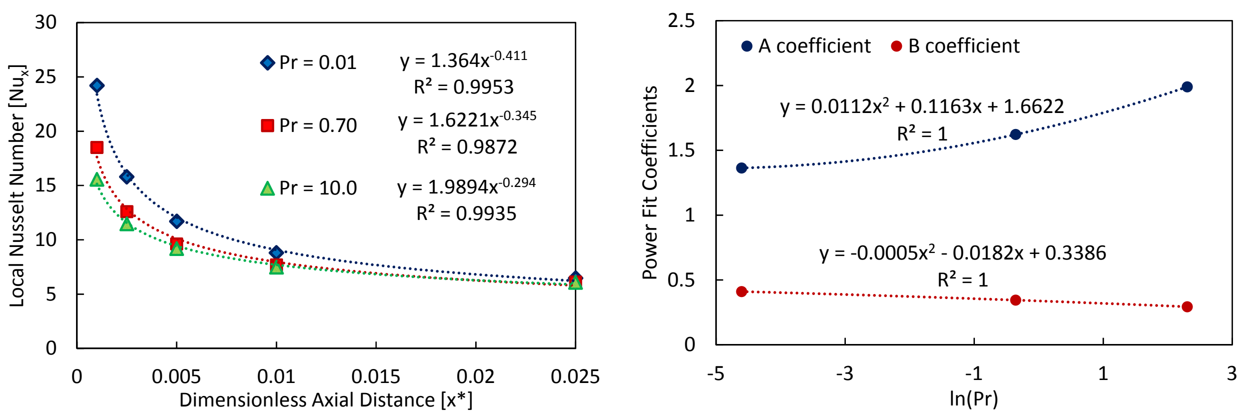

(a) Nusselt number vs x^* (b) Coefficients vs Pr

Figure 4.8: Development of Nusselt number fit curve

Nu_x was fit to an equation of the form $Nu_x = A\left(x^*\right)^{-B}$ and the resulting A and B coefficients were fit to an equation of the form $y = C_1 \left(\ln Pr\right)^2 + C_2 \left(\ln Pr\right) + C3$. The resulting equation for the local Nusselt number is given by

$$Nu_x = A\left(x^*\right)^{-B} \tag{4.19}$$

where

$$A = 0.0112\,(\ln Pr)^2 + 0.1163\,(\ln Pr) + 1.6622 \tag{4.20}$$

$$B = -0.0005\,(\ln Pr)^2 - 0.0182\,(\ln Pr) + 0.3386 \tag{4.21}$$

The average Nusselt number for the bottom surface is then found by averaging over the surface using

$$\overline{Nu_{\mathrm{D}}} = \frac{\int_0^{x^*} Nu_x dx}{x^*} \tag{4.22}$$

The heat transfer from the bottom surface is then evaluated using the mean gas temperature $\overline{T_{\mathrm{g}}}$ given by

$$\overline{T_{\mathrm{g}}} = \frac{T_{\mathrm{t}} + T_{\mathrm{p}}}{2} \tag{4.23}$$

4.3.4 Effective Heat Transfer Coefficient

In order to incorporate radiation while maintaining linear equations, an effective heat transfer coefficient is used between the tube surfaces and the particle flow as shown below.

$$h_{\mathrm{eff}} = h_{\mathrm{conv}} + \frac{\sigma\left(e_{\mathrm{t}} T_{\mathrm{t}}^4 - e_c T_{\mathrm{p}}^4\right)}{T_{\mathrm{t}} - T_p} \tag{4.24}$$

where h_{conv} is the convective heat transfer coefficient, T_{t} is the temperature of the adjacent tube surface, T_{p} is the particle temperature, e_{t} is the emissivity of the adjacent tube surface and e_{c} is the emissivity of the particle curtain. The curtain emissivity differs from that of the raw material due to changes in transmissivity and is calculated by [47]

$$e_{\mathrm{c}} = e_{\mathrm{p}}\,(1 - \tau_{\mathrm{c}}) \tag{4.25}$$

where τ_{c} is the transmissivity of the curtain given by

$$\tau_c = \exp\left(-\frac{3\epsilon}{2d_{\mathrm{p}}} z_{\mathrm{c}}\right) \tag{4.26}$$

where ϵ is the solids volume fraction of the particle curtain, d_p is the particle size and z_{c} is the curtain thickness defined by the depth of the flow, d.

4.3.5 Particle Phase Conductivity

The bulk conductivity of the granular phase is an important parameter in many of the correlations used for analysis. This can be calculated using the Maxwell model [48]

$$k = \frac{\gamma k_{\mathrm{g}} \left(2k_{\mathrm{g}} + k_{\mathrm{s}}\right) + 3\epsilon k_{\mathrm{s}} k_{\mathrm{g}}}{\gamma \left(2k_{\mathrm{g}} + k_{\mathrm{s}}\right) + 3\epsilon k_{\mathrm{g}}} \tag{4.27}$$

$$\epsilon = 1 - \gamma \tag{4.28}$$

where k is the bulk conductivity of the granular phase, k_{s} is the conductivity of the solid material, k_{g} is the conductivity of the interstitial gas phase, ϵ is the solids volume fraction and γ is the gas volume fraction within the particle flow. This model gives the closest match to experimental results using foundry sand of the models considered by Malherbe [48]. The gas conductivity is that of air and is given in W/m-K using using T_{g} in Kelvin by

$$k_{\mathrm{g}} = 1.5207 \times 10^{-11} T_{\mathrm{g}}^3 - 4.8574 \times 10^{-8} T_{\mathrm{g}}^2 + 1.0184 \times 10^{-4} T_{\mathrm{g}} - 3.9333 \times 10^{-4} \tag{4.29}$$

4.4 1D Granular Flow Modeling

In order to calculate the parameters needed to predict the heat transfer coefficients, the granular flow dynamics were also modeled. This was done by assuming one-dimensional flow through the receiver section under consideration using control volumes as shown in Figure 4.9. Although this appears to be a significant assumption, the existing literature on granular flows over plates, as discussed in the literature review, concludes that the volume fraction and velocity profiles through the depth of such a flow are nearly constant [38–40].

The parameters of interest are the solids volume fraction, the depth of the particle flow, the average particle velocity, the particle temperature, the average gas velocity and the gas temperature. In order to simplify the problem, it was assumed that the gas temperature equals the particle temperature for a given node since the phases are highly intermixed and both subject to heating. It was further assumed that the system operates under constant pressure and air was treated as an ideal gas.

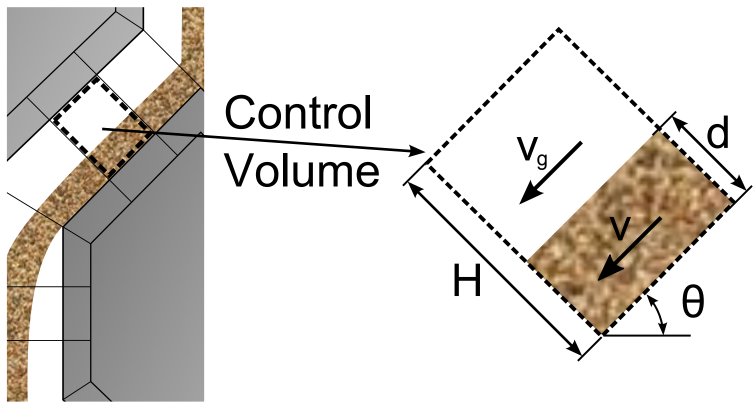

Figure 4.9: Control volume for particle flow nodes with relevant variables and parameters

Other studies modeling granular flows down inclines treat the volume fraction as a constant and allow the flow depth to change as the particles accelerate [41, 42]. This approach was followed for the top tube surfaces. For the vertical channels, the experimental results show that the particles spread out and do not have a well defined flow depth. For these channels, it was assumed that the flow depth is equal to the height of the channel and the average solids volume fraction was allowed to vary as the particles accelerate. The remaining 4 state variables were found using equations for conservation of mass, momentum and energy for the particles and conservation of mass for the gas.

4.4.1 Solid Phase Continuity

The solid phase continuity equation at steady state takes the form

$$\frac{\partial}{\partial x}\left(\epsilon \rho_{\mathrm{s}} d v\right) = 0 \tag{4.30}$$

where ϵ is the average solids volume fraction over the depth of the particle flow, v is the average particle velocity parallel to the tube wall, d is the particle flow depth and ρ_{s} is the density of the solids material. The bulk density is therefore defined by $\rho_{\mathrm{s}}\epsilon$.

The discretized solids phase continuity equation for a control volume at node i can be written

$$0 = \rho_{\mathrm{s}} \epsilon_{i-1} v_{i-1} L_{\mathrm{t}} d_{i-1} - \rho_{\mathrm{s}} \epsilon_i L_{\mathrm{t}} d_i v_i \tag{4.31}$$

where L_t denotes the length of the receiver tube and $L_\mathrm{t}d$ gives the cross-sectional area of the particle flow.

4.4.2 Solid Phase Momentum

The solids momentum equation is given by

$$\underbrace{\frac{\partial}{\partial x}\left(\epsilon\rho_\mathrm{s} d v^2\right)}_{\text{momentum flux}} = \underbrace{\epsilon\rho_\mathrm{s} d g \sin\theta}_{\text{gravity}} - \underbrace{\epsilon\rho_\mathrm{s} d g \cos\theta \tan\delta}_{\text{wall friction}} - \underbrace{d\beta_\mathrm{v}\left(v - v_g\right)}_{\text{particle-air drag}} \tag{4.32}$$

where θ is the inclination angle of the surface from the horizontal, δ is the bed friction angle which is defined as the minimum inclination angle needed for a layer of particles to flow over the surface, v_g is the gas velocity and β_v is the drag coefficient. The drag coefficient can be calculated from the Ergun equation [49, 50] by

$$\beta_\mathrm{v} = 150\frac{\left(1-\gamma\right)^2 \mu_\mathrm{g}}{\gamma\left(d_\mathrm{p}\phi_\mathrm{s}\right)^2} + 1.75\frac{\rho_\mathrm{g}\left|v_\mathrm{g} - v\right|\left(1-\gamma\right)}{\phi_\mathrm{s} d_\mathrm{p}} \tag{4.33}$$

where μ_g is the gas viscosity, ρ_g is the gas density, d_p is the particle diameter and ϕ_s is the particle sphericity which is assumed to be unity. The gas viscosity is that of air and is given in kg/s-m using T_g in Kelvin by

$$\mu_\mathrm{g} = 2.84450^{-6} + 5.9996\times10^{-8}T_\mathrm{g} - 2.6725\times10^{-11}T_\mathrm{g}^2 + 7.1510\times10^{-15}T_\mathrm{g}^3; \tag{4.34}$$

The discretized form of the momentum equation for a control volume becomes

$$\begin{aligned} 0 = {} & \rho_\mathrm{s} L_\mathrm{t} d_{i-1}\epsilon_{i-1}v_{i-1}^2\cos\left(\left|\theta_{i-1}-\theta_i\right|\right) - \rho_\mathrm{s} L_\mathrm{t} d_i \epsilon_i v_i^2 \\ & + dx L_\mathrm{t} d_i \rho_\mathrm{s}\epsilon_i g \sin\left(\theta\right) - \tan(\delta)\, dx L_\mathrm{t}\left(d_i\rho_\mathrm{s}\epsilon_i g\cos\left(\theta\right)\right) - dx L_\mathrm{t} d_i \beta_v\left(v_i - v_{g,i}\right) \end{aligned} \tag{4.35}$$

where dx is the length of each node in the flow direction and the addition of $\cos\left(\left|\theta_{i-1}-\theta_i\right|\right)$ on the incoming solids momentum accounts for losses due to inelastic collisions as the particles change direction at the tube corners. When transitioning from an inclined channel to a vertical channel the particles impact each other, and when transitioning back to an inclined channel the particles impact the surface of the next tube. It should be noted that other models of granular flow down inclines include an additional rate-dependent friction term

[41, 42]. This was neglected in this analysis because the direction changes throughout the flow regime dominate the maximum velocity obtained.

4.4.3 Gas Phase Continuity

The gas phase continuity equation is written as

$$\frac{\partial}{\partial x}\left(\left(H-\epsilon d\right)\rho_{\mathrm{g}} v_{\mathrm{g}}\right)=0 \tag{4.36}$$

where H is the height of the particle flow channel and $(H - \epsilon d)$ represents the gas volume fraction throughout the entire channel volume. The channel height must be included because it is not constant throughout the array.

The discretized form is written

$$0 = L\rho_{\mathrm{g},i-1}\left(H-\epsilon d_{i-1}\right)v_{\mathrm{g},i-1} - L\rho_{\mathrm{g},i}\left(H-\epsilon d_{i}\right)v_{\mathrm{g},i} \tag{4.37}$$

where the gas density is calculated using the ideal gas law and the gas is again assumed to be at the same temperature as the particles.

4.4.4 Solid Phase Energy

The solid phase, steady state energy balance is given by

$$\bar{c}_{\mathrm{p}}\frac{\partial}{\partial x}\left(T_{\mathrm{p}}\right)+\dot{q}=0 \tag{4.38}$$

where $\bar{c}_{\mathrm{p}}$ is the average specific heat of the particles and $\dot{q}$ is the volumetric energy input.

This can be written for a control volume as

$$0 = L_{\mathrm{t}} d_{i-1}\rho\epsilon_{i-1}v_{i-1}\bar{c}_{\mathrm{p}}T_{\mathrm{p},i-1} - L_{\mathrm{t}} d_{i}\rho\epsilon_{i}v_{i}\bar{c}_{\mathrm{p}}T_{\mathrm{p},i} + h_{\mathrm{eff,W1}}\left(T_{\mathrm{W1}}-T_{\mathrm{p},i}\right)dxL_{\mathrm{t}} + h_{\mathrm{eff,W2}}\left(T_{\mathrm{W2}}-T_{\mathrm{p},i}\right)dxL_{\mathrm{t}} \tag{4.39}$$

where there is heat input from the walls above and below the given particle node denoted by subscripts W1 and W2. The temperatures are those of the adjacent tube nodes and the heat transfer coefficients are evaluated by the previously discussed correlations and include both convective and radiative contributions.

The particle specific heat is taken to be that of pure silica which differs only slightly from alumina over the temperature range of interest. An equation was developed based on data found in [51] and is given by

$$c_{\mathrm{p}} = 138.5667(4.871 + 0.005365T_{\mathrm{p}} - 100100T_{\mathrm{p}}^{-2}) \tag{4.40}$$

where c_{p} is given in J/kg-K using T_{p} in Kelvin

4.4.5 Inlet Conditions

The inlet conditions are established by first setting the particle mass flow rate. Particles then enter as if from a hopper and are assumed to fill the entire volume of the channel along the top face of the first tube at the set constant solids volume fraction. The initial particle velocity is then calculated to realize the desired mass flow rate. Air fills the remaining volume and enters at the same velocity as the particles.

4.5 Input Parameter Selection Based on Comparison to Experimental Data

Several of the parameters needed for the equations discussed above remain unknown. These are the flowing solids volume fraction along the top tube face, the bed friction angle and the "effective" film thickness for the side face. These values were selected through comparison with the experimental data at maximum flow conditions for the 300 µm particle batch. The model was set to simulate the experiments by using the parameters in Table 4.1. These were chosen to mimic solid aluminum tubes operated at moderate power.

4.5.1 Particle Flow Depth Considerations

One of the important parameters that must be considered in validating the model is the depth of the particle flow over the top surface of the tubes. The simulation results, see Figure 4.10, show that the particles accelerate along the top tube surfaces and in the vertical channels before decreasing in velocity at the corners. The particle flow depth follows the inverse of the velocity along the top tube surfaces. In reality, the maximum height of the particle flow is constrained by the physical dimensions of the system.

Table 4.1: Input parameters for comparison to experimental data

Parameter	Symbol	Input Value
Mass flow rate per channel	$\dot{m}$	0.43 kg/s
Tube wall thickness	t_{t}	0.30 in
Tube inner wall emissivity	e_{t}	0
Particle material emissivity	e_{p}	0.8
Particle tube surface emissivity	e_{t}	0.2
Tube material conductivity	k_{t}	167 W/m-K
Particle diameter	d_{p}	300 µm
Particle inlet temperature	$T_{\mathrm{p},0}$	25°C
Solar flux	q''_{solar}	440 W/m^2
Tube rows	R	5

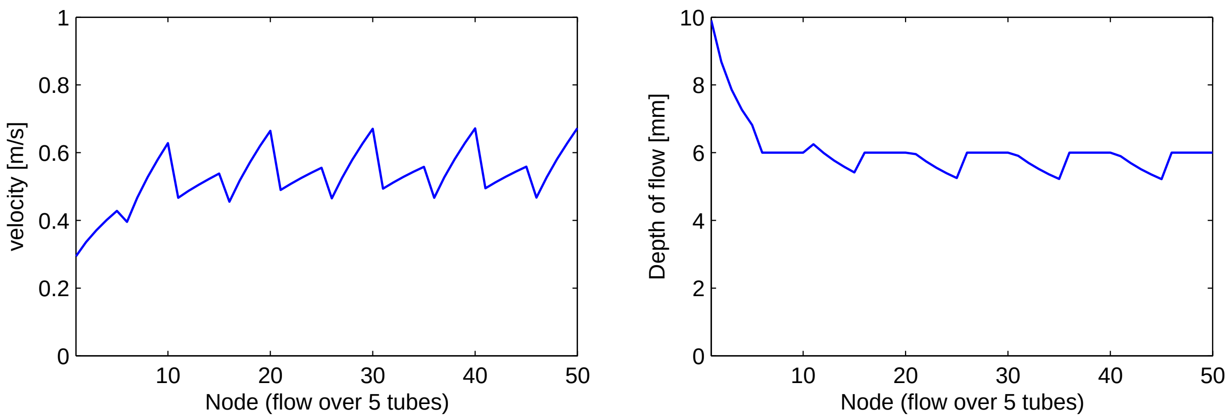

(a) Particle velocity vs node

(b) Flow depth vs node

Figure 4.10: Sample results

As previously mentioned, see Figure 3.4, the distance between each tube face in the experimental array is the same, but the simulation considers a channel containing only half of a tube width. Therefore, the height of the vertical channel within the simulation is half the height of the inclined channel along the top face. In order for the flow to fit within these constraints, the flow along the top surface must fill less than half of the channel height when it reaches the entrance to the vertical channel. The input parameters that affect the flow depth are the solids volume fraction along the top face and the bed friction angle. Figure 4.11(a) shows the limiting flow depth over the first tube where the flow is slower and Figure 4.11(b) shows the flow depth at the end of the top face for a tube farther down the array where steady state conditions have been reached as functions of the relevant parameters. The flow depth decreases with increasing solids volume fraction and decreasing friction angle. The dashed line shows the maximum height that can fit the geometry. Points below this line represent possible solids volume fraction and friction angle combinations that could be selected.

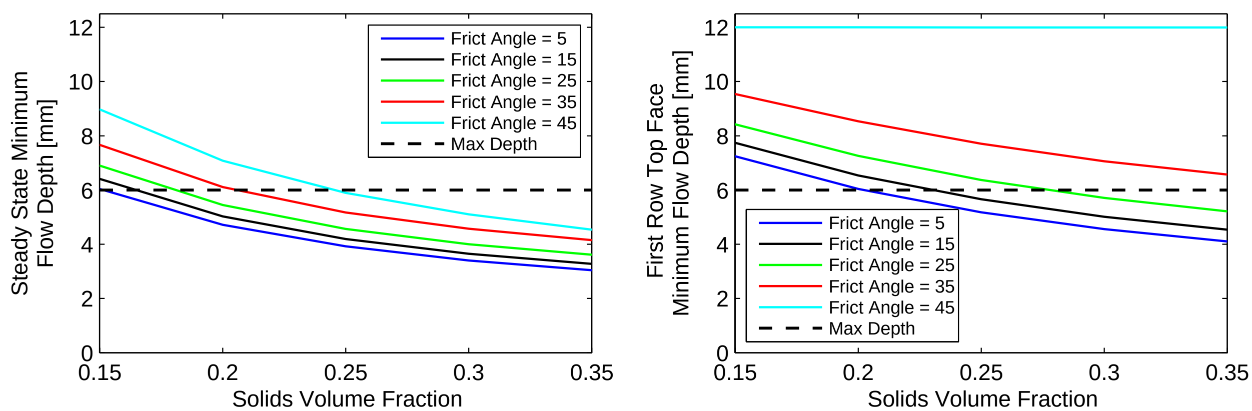

(a) Entrance region min flow depth

(b) Steady state minimum flow depth

Figure 4.11: Flow depth considerations at maximum flow conditions

4.5.2 Heat Transfer Considerations

The effective heat transfer coefficient across the side face as a function of the “effective” film thickness is shown in Figure 4.12 along with the experimental data. The effective heat transfer coefficient is taken from the simulation for direct comparison to the experimental results that include all modes of heat transfer. The solid horizontal line represents the mean of the experimental results and the dashed lines represent 1 and 2 standard deviations from the mean. Simulations showed that only the “effective” film thickness has significant impact on the side face HTC. Decreasing the “effective” film thickness increases this heat transfer coefficient.

The bottom face heat transfer coefficient is dependent upon the solids volume fraction and the bed friction angle as these impact the flow depth and therefore the thickness of

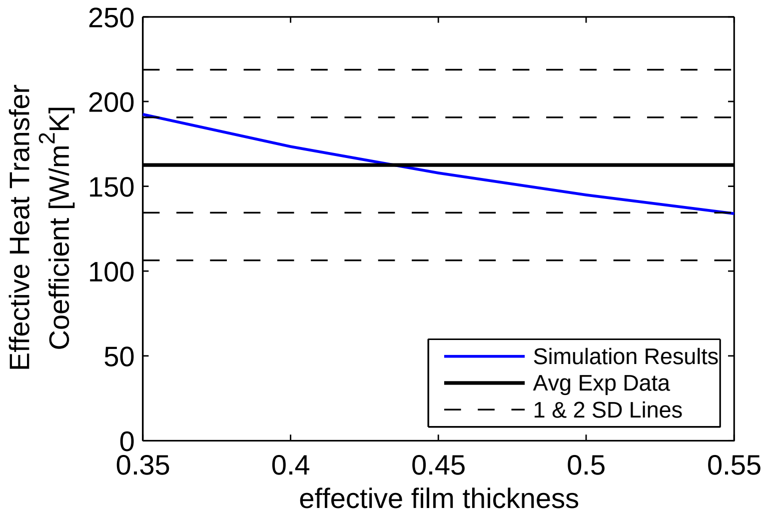

Figure 4.12: Side face heat transfer analysis vs the relevant parameters

the air channel along the bottom surface. Changes in heat transfer with these parameters are shown in Figure 4.13 along with the average experimental value and lines for 1 and 2 standard deviations from the mean. Heat transfer increases with decreases in the solids volume fraction and with increases in the bed friction angle.

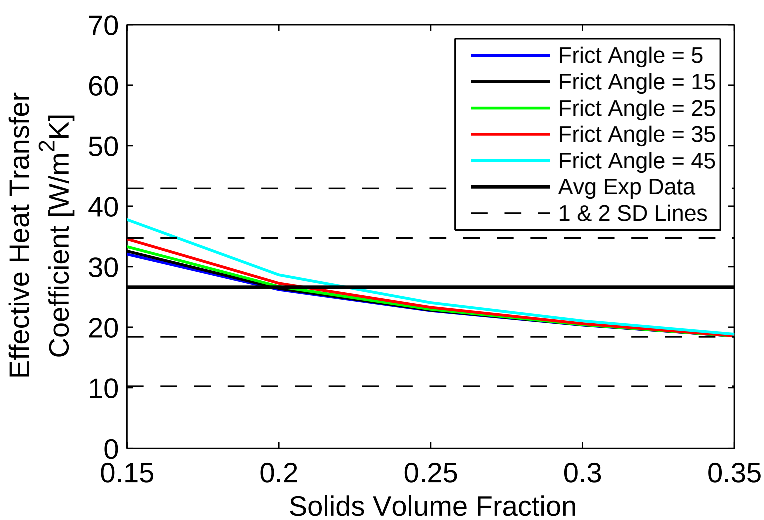

Figure 4.13: Bottom face heat transfer analysis vs the relevant parameters

Heat transfer across the top surface is also impacted by the solids volume fraction and the bed friction angle, see Figure 4.14. Here the heat transfer also increases with increased bed friction angle, but unlike the bottom face, increases with increased solids volume fraction.

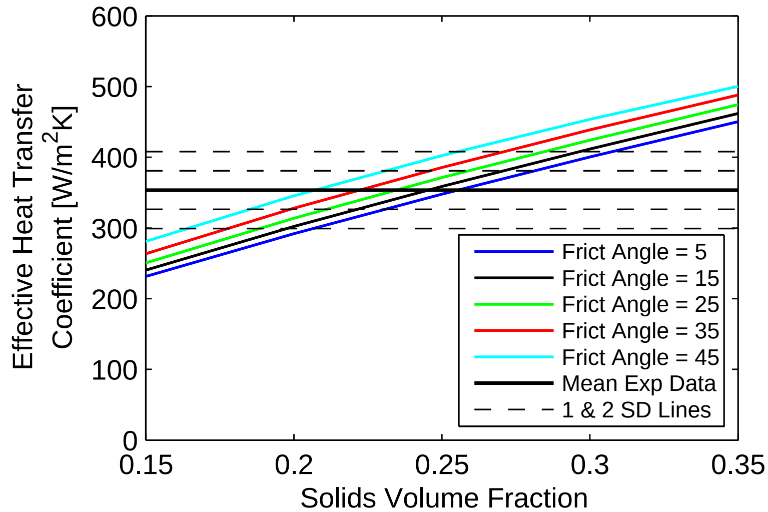

Figure 4.14: Top face heat transfer analysis vs the relevant parameters

4.5.3 Parameter Selection

The value of the "effective" film thickness affects the side face heat transfer coefficient only and this heat transfer is scarcely affected by any other parameters. A value of $x_{\text{eff}} = 0.43$ was therefore chosen to best match the average heat transfer coefficient from the experimental results. Figure 4.12 shows that any value in the range of 0.4-0.5 could feasibly be chosen.

In order to select the appropriate values for the bed friction angle and the solids volume fraction, the particle flow depth and top and bottom heat transfer coefficients must all be taken into account. This was done through the use of the mutli-layered contour plot shown in Figure 4.15. The gray shaded areas represent those that are satisfactory according to the flow depth considerations with the darker areas being more preferable. The requirements have been set at $d < 6$ mm for the steady state flow and $d < 1.1 \times 6$ mm to give a 10% tolerance for the first tube where the slower and more densely packed flow conditions may cause the solids volume fraction to increase. The blue and red shaded areas represent the acceptable regions for the heat transfer from the top and bottom surfaces, respectively, and are centered about the mean. The darker area for each color represents values within ±10% of the average experimental value and the lighter area represents ±15%. ±15% is approximately the 2σ window for the top face but represents a much tighter tolerance on the bottom face. Where all of the darker areas overlap, as outlined by the solid black lines, represents the best fit window according to the data collected. This window is biased towards meeting the top face value and includes the 15% deviation range for the bottom face heat transfer. The exact values selected were $\epsilon = 0.25$ and $\delta = 20^\circ$ as these were found to give the best results of those within the acceptable window. The acceptable range and the values selected are further outlined in Table 4.2.

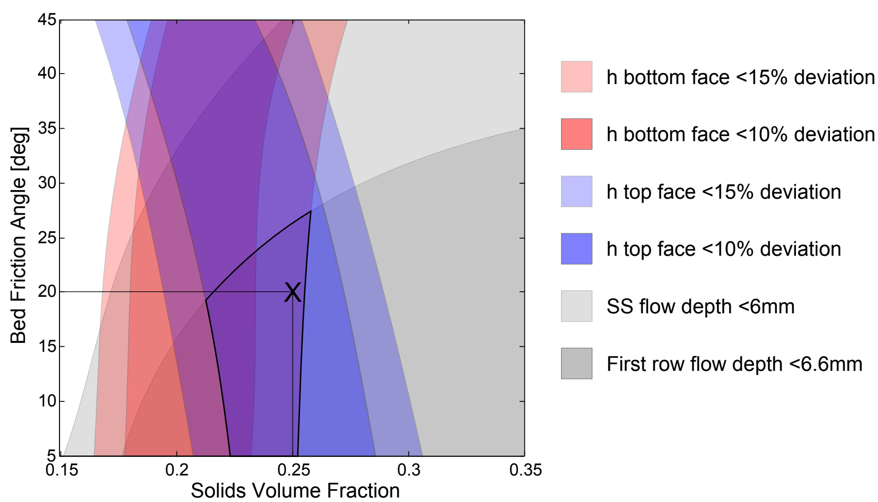

Figure 4.15: All considerations for parameter selection

Table 4.2: Acceptable parameter inputs based on comparison to experimental data

Parameter	Symbol	Acceptable Range	Value Chosen
Solids volume fraction	ϵ	$0.20 - 0.30$	0.25
Side face "effective" film thickness	x_{eff}	$0.40 - 0.5$	0.43
Bed friction coefficient	δ	$5^\circ - 25^\circ$	20°

4.6 Model Validation

A more thorough validation of the model can be performed through analysis of the results incorporating the final parameters selected. As shown in Figure 4.16, the particle flow depth decreases to the required 6 mm before reaching the first vertical segment and for each subsequent vertical channel. Additionally, the flow depth decreases along each top tube surface in agreement with the flow observed in the experiments.

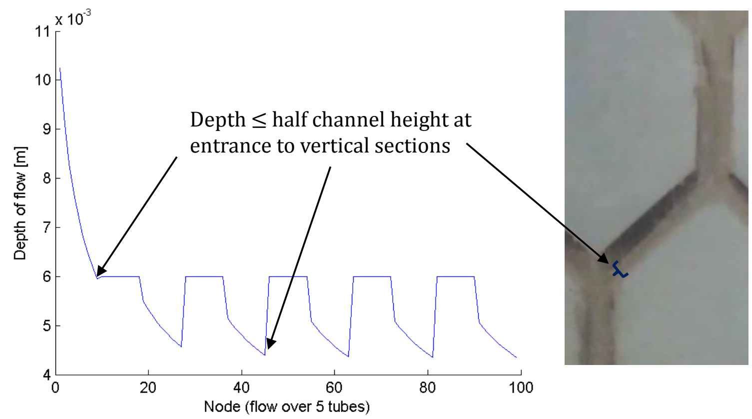

Figure 4.16: Flow depth considerations

The heat transfer results can also be compared to the experimental data as a function of mass flow rate. This is shown for the 300 µm particle batch in Figure 4.17 and for the 200 µm batch in both Figure 4.18 and Figure 4.19.

From the 300 µm batch we can see that the data is well represented by the simulation. At the maximum flow rate, the simulation results match the average experimental results very closely. The simulation accurately captures the slight decrease in heat transfer with decreased mass flow rate for the bottom surface across the range examined. The decrease in the top face heat transfer coefficient with decreasing flow rate is also captured by the model except for the dramatic decrease at the lowest mass flow rate. Heat transfer from the side face shows a dip at moderate mass flow rates before increasing to a value slightly less than or equal to those seen at the highest mass flow rate. The simulation predicts a slight decrease in heat transfer with decreasing mass flow rate that follows the average well but does not

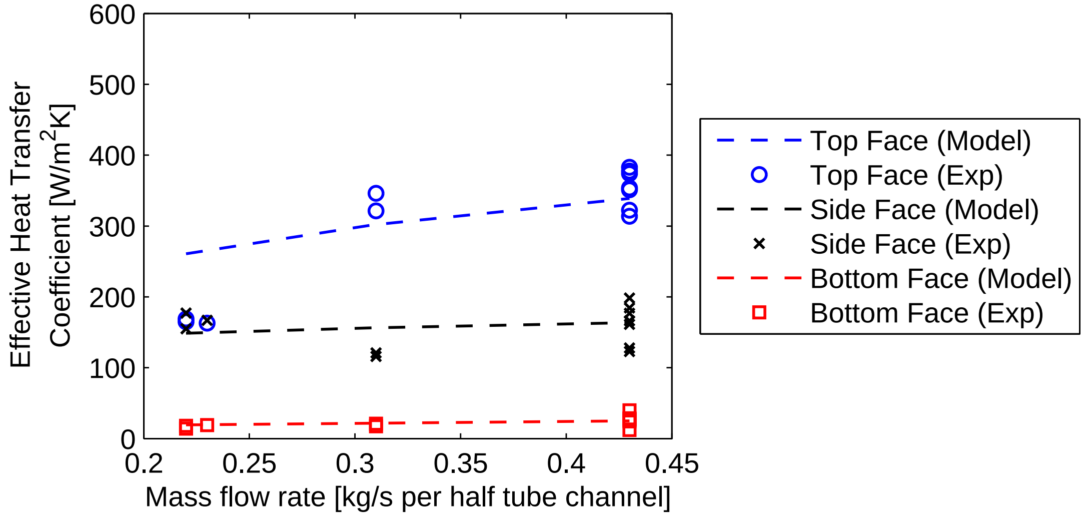

Figure 4.17: 300 micron simulation vs 300 µm particle batch data

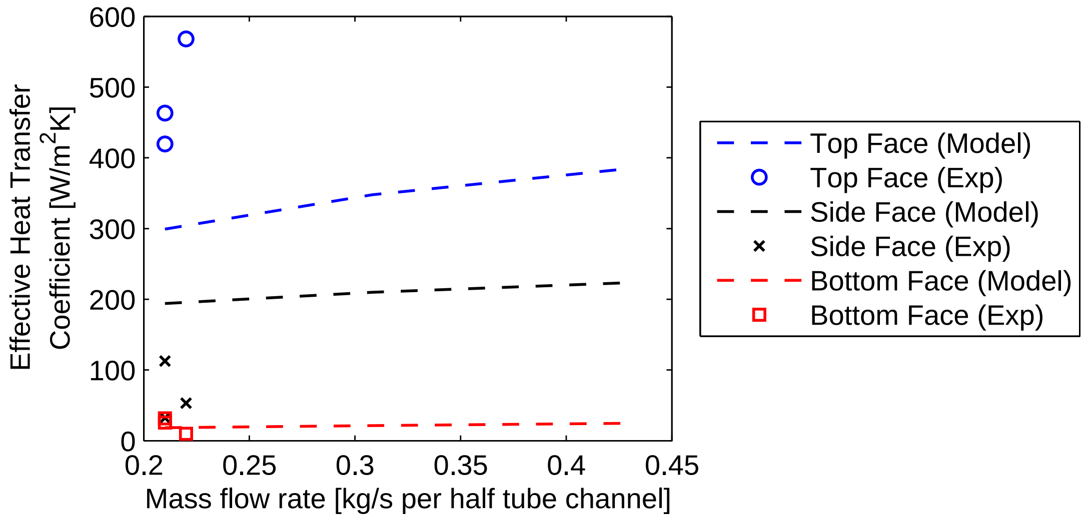

Figure 4.18: 200 micron simulation vs 200 µm particle batch data

accurately capture the slight dip at moderate flow rates.

Simulations of the 200 µm batch show that the results are more accurately predicted for the top face using 100 µm particles in the model. Heat transfer coefficients do not differ between results for the bottom face and are well captured in either case. Heat transfer for the side face is only moderately well captured by the use of 200 µm particles and appears to be more erroneous using 100 µm particles.

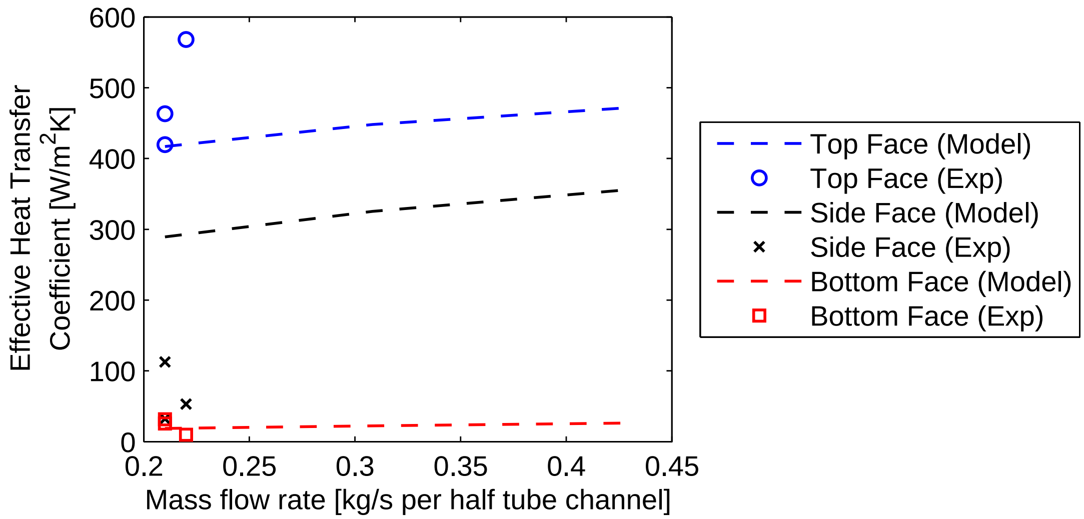

Figure 4.19: 100 micron simulation vs 200 µm particle batch data

4.7 Numerical Parameters

It is also important to discuss the numerical considerations of the model. The temperature residual criteria governs convergence for the iterative solver and is defined by

$$\Delta T_{\text{res}} = \frac{T_{\text{c}} - T_{\text{prev}}}{T_{\text{prev}}} \tag{4.41}$$

where T_{c} is the current temperature value and T_{prev} is the value from the previous iteration for a given tube or particle flow node temperature. The other important parameter is the mesh sizing which is set by N_{face}, the number of nodes for each face of each tube. The results for the particle outlet temperature and the maximum tube temperature vs N_{face} are shown in Figure 4.20(a) and Figure 4.20(b) for three different temperature residual criteria from a simulation of 30 rows of tubes and are representative of the trends seen in other parameters. The ordinate is the normalized difference between the value for the given case and the value predicted for $N_{\text{face}} = 11$ with $\Delta T_{\text{res}} = 1E\text{-}5$.

These graphs show that the overall outlet temperature predicted by the model is scarcely affected by the number of nodes as long as $\Delta T_{\text{res}} < 1E\text{-}4$. Additionally, the maximum tube temperature accuracy improves with increased node count but only moderately improves

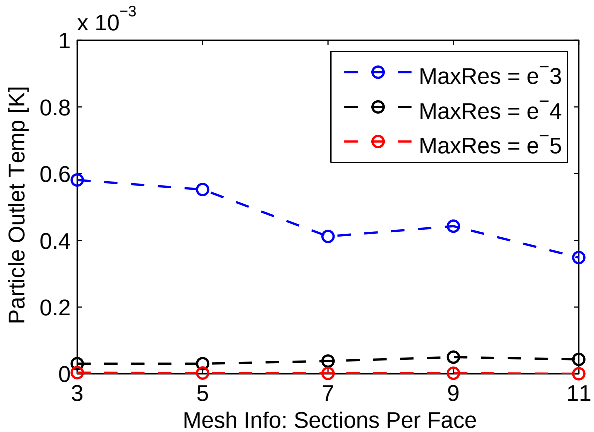

(a) Entrance region minimum flow depth

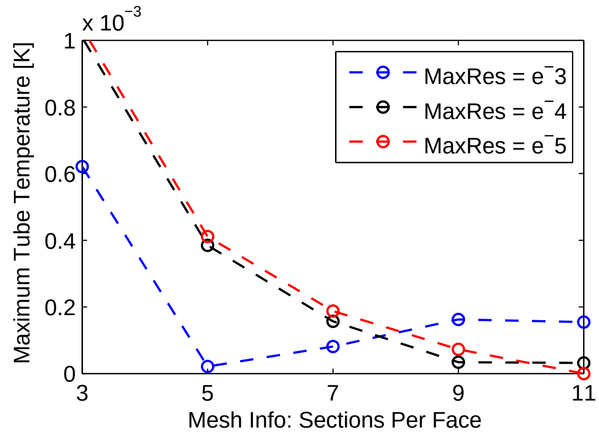

(b) Steady state minimum flow depth

Figure 4.20: Numerical Parameters Comparison

with increases in ΔT_{res} beyond $1E$-4. In order to maximize return on computational investment and to allow runs to complete in a reasonable timeframe, all runs utilized $\Delta T_{\text{res}} = 1E$-4 while runs using hundreds of tube rows used $N_{\text{face}} = 5$ and shorter runs used $N_{\text{face}} = 7$ or 9.

4.8 Discussion

Overall, the results show that the experimental results are well represented by the model. In particular, the heat transfer coefficients predicted by the model are very good at the high mass flow rates utilized in its development and capture many of the trends seen for decreasing flow rates. The side wall heat transfer is the most poorly predicted value for both particle sizes. This is likely due to the complex and dynamic nature of the flow in this region of the receiver that is not entirely captured. Additionally, the use of a single constant to define the "effective" film thickness is likely oversimplified. This parameter should depend upon other parameters such as the mass flow rate and the average solids volume fraction across the channel. Literature on heat transfer models using the kinetic theory of gases and for heat transfer in pneumatically conveying particles shows the presence of critical velocity and volume fractions that could at least partially explain the trends seen for the side wall.

The values chosen for the solids volume fraction and the bed friction angle represent the best fit given the experimental data. As this data contains significant variability, the selected parameters do not necessarily represent the exact physical parameters from the experiment. A range of input parameters could have been selected that would fit the data within an acceptable tolerance. More in-depth experiments could measure these parameters directly.

The heat transfer correlations developed make the inherent assumption of constant particle sizes. Comparison with experimental data shows that the presence of a mixture of particle sizes can significantly vary the results. The 200 μm particle batch exemplifies heat transfer characteristics more fitting of 100 μm sized particles. This is likely due to improved contact at the particle surface due to the presence of fine particles within the particle batch. This is not seen with the 300 μm particle batch as the particle size is more tightly controlled.

CHAPTER 5

RECEIVER ANALYSIS

The promising accuracy of the simplified model developed in the previous chapter gives confidence in its use for analyzing the full-size receiver. The performance of the full system can be analyzed using this model in a variety of ways. First, the equations developed, such as the heat transfer correlations, can be analyzed directly to see the impact of various parameters. Additionally, a full-sized receiver can be simulated at high temperature that includes radiation on the solar side of the tubes and uses the expected operational parameters. Temperatures and energy flows within the system can then be analyzed.

5.1 Heat Transfer Correlation Analysis

Here the primary parameters and variables that affect the heat transfer coefficients, the particle flow depth, velocity and solids volume fraction, have been varied in order to study the effects on the heat transfer correlations directly, see Figure 5.1. For these simulations the gas velocity was set equal to the particle velocity. It should also be noted that these simulations vary the parameters only and are not directly comparable between data points. For example, increasing the velocity or solids volume fraction while maintaining a constant velocity also leads to an increase in the average mass flow rate. Thus, the trends may be examined but a given set of conditions may not be obtainable in the design.

From these graphs several trends can be observed for each of the faces. First, the bottom face heat transfer is not directly dependent upon the solids volume fraction but does increase slightly with both depth and gas velocity. Increased gas velocity increases the Reynolds number, which leads to an increase in the entry length, and thus increases the average Nusselt number and HTC for this face. The heat transfer coefficient is also dependent upon the inverse of the air channel thickness, therefore, when the particle depth increases, the air channel thins and the HTC increases.

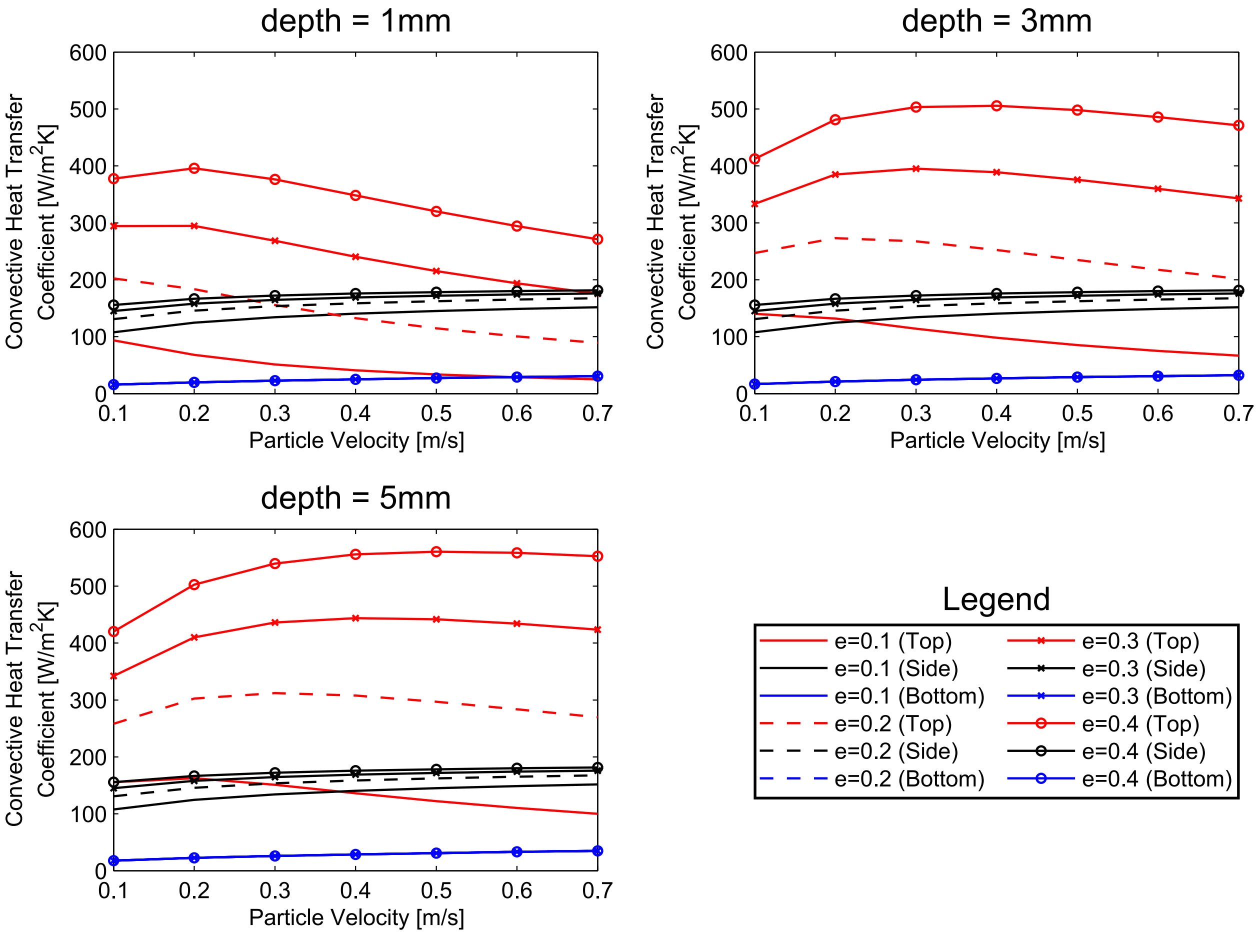

Figure 5.1: Direct heat transfer correlation analysis results

The side face heat transfer correlation shows increases in the HTC with increases in both velocity and solids volume fraction over the entire range of parameters studied. This is due to the direct dependence of the Peclet number on the velocity and the particle phase conductivity and the dependence of conductivity on the solids volume fraction. Increased solids volume fraction decreases the distance between particles and improves bulk conductivity leading to an improved HTC. The heat transfer coefficient from the side face has no direct dependence on the particle flow depth.

The HTC for the top face is very dynamic over the range of parameters studied and is significantly dependent upon each of them. The heat transfer coefficient for the top face shows a maximum at a critical velocity that is unique for each set of other parameters. This maximum is caused by the unique dependence of both the Peclet and Froude numbers on the velocity. Largely due to the aforementioned improvements in particle phase conductivity, the most significant increases in the HTC are caused by increasing the solids volume fraction. Increasing the depth also increases the HTC as it decreases the Froude number.

5.2 Full Receiver Simulations

As previously mentioned, a significant advantage of this simplified model is its ability to simulate a full-scale receiver. This was done using the input conditions and parameters outlined in Table 5.1. These parameters incorporate the thin walls that would be needed for a functional absorber tube and the temperature-dependent conductivity for stainless steel. The particle side emissivity is set to that of stainless steel and the solar side is set for a highly reflective material that would be needed to obtain appropriate solar flux spreading along the length of the tube. The solids volume fraction, bed friction angle and side wall "effective" film thickness utilize the parameters developed in the preceding chapter.

Table 5.1: Input parameters used for full NBB receiver simulation

Parameter	Symbol	Input Value
Solids volume fraction	ϵ	0.25
Side face "effective" film thickness	x_{eff}	0.43
Bed friction coefficient	δ	20°
Solids mass flow rate	$\dot{m}$	0.5 kg/s
Tube wall thickness	t_{t}	1/16 in
Solid particle material density	ρ_{s}	2700 kg/m^3
Solid particle material conductivity	k_{s}	1.5 W/m-K
Tube solar side emissivity	e_{in}	0.15
Tube particle side surface emissivity	e_{t}	0.8
Particle material emissivity	e_{p}	0.8
Particle diameter	d_{p}	300 µm
Particle sphericity	ϕ_{s}	1
Particle inlet temperature	$T_{\mathrm{p,0}}$	300°C
Ambient air temperature	T_{amb}	35°C
Operating pressure	P	1 atm
Solar flux	q''_{solar}	1000 W/m^2
Tube rows	R	500 rows
Solar magnification		1000 suns

5.2.1 Particle Flow Results

The local results, see Figure 5.2, show the steady state behavior of both the particles and the gas phase through the channels of the array. As discussed previously, the particles accelerate along the top, inclined face of the tubes and in the vertical sections between tubes before losing speed due to inelastic collisions as they turn the corners between the channel sections. As the particles accelerate, the depth and solids volume fraction decrease for the top and side faces, respectively. The gas velocity also oscillates between channels.

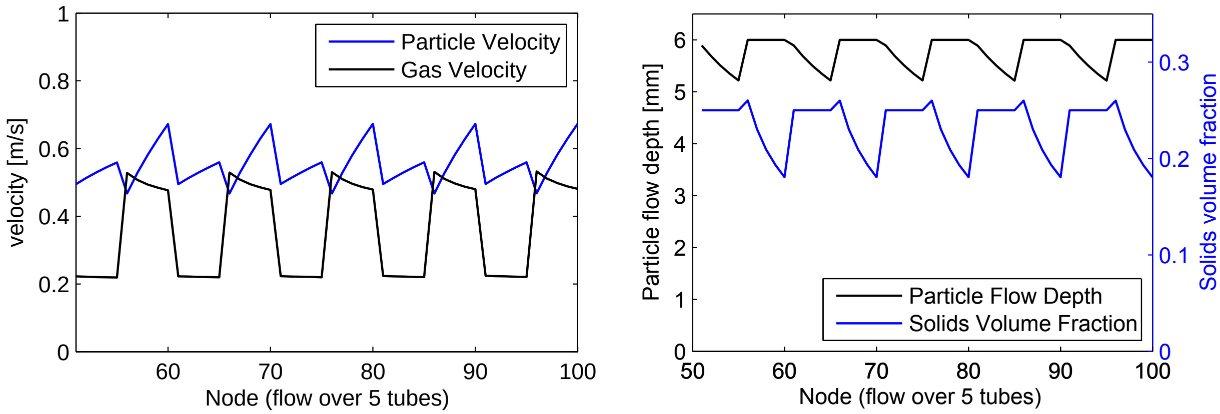

(a) Particle and gas velocities vs node

(b) Flow depth vs node

Figure 5.2: Fully developed particle flow dynamics results

The overall average flow results for each tube, differentiated by channel type, are shown in Figure 5.3. It can be seen that the average gas velocity increases along the rows of the receiver. Average particle velocity also increases through the height of the receiver but much more slowly. The average depth in the inclined channels and the average solids volume fraction in the vertical channels decrease with the increases in average velocity.

5.2.2 Heat Transfer Results

The average temperature for each tube within the receiver as well as the temperature of the particles leaving that row are given in Figure 5.4 along with the local temperature results for selected tubes. As intended, the particle temperature increases down the rows of

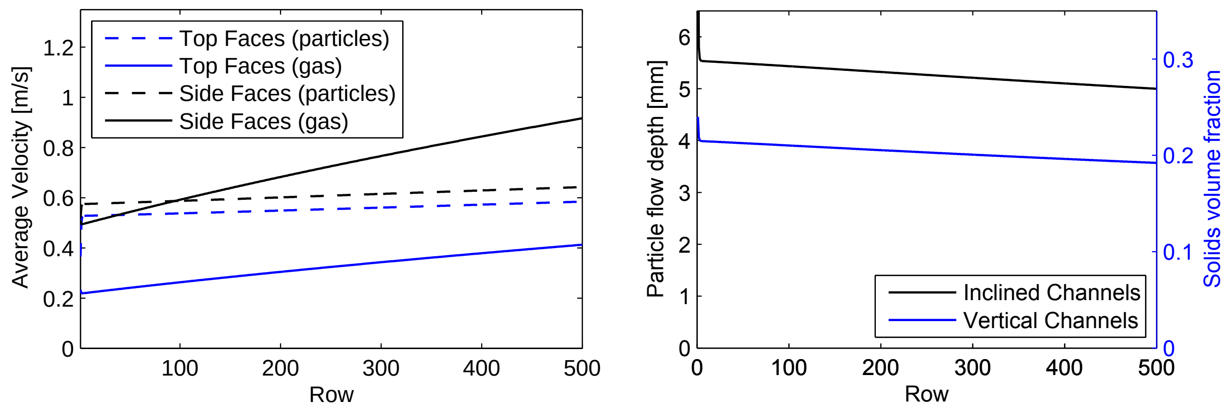

(a) Particle and air velocities

(b) Particle flow depth

Figure 5.3: Average flow conditions

the receiver. Consequently, the average tube temperature also increases and is always higher than the particle temperature. The difference between these two temperatures decreases along the receiver height. Tube node temperatures are presented as the node temperature minus the average tube temperature. Negative values therefore indicate nodes that are cooler than the average. The results show that the top vertex is the coolest node and the temperature increases along the perimeter towards the bottom vertex. The range of node temperatures seen on a single tube decreases as the average temperatures increase.

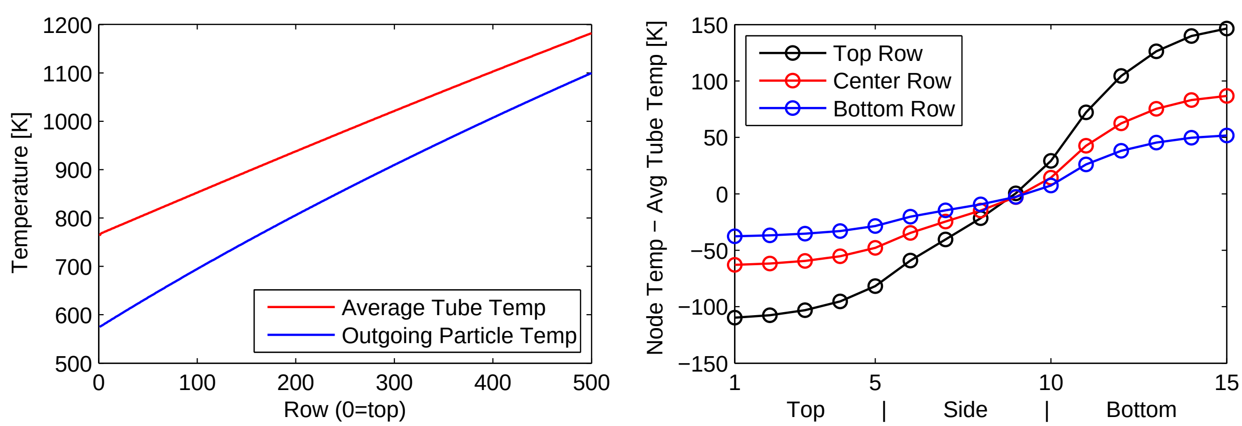

(a) Average temperatures by row

(b) Normalized nodal tube temperatures

Figure 5.4: Temperature results

The average heat transfer coefficient for each face by row is given in Figure 5.5 for the full-sized receiver. Here we can clearly see that the heat transfer coefficients are significantly higher for each face at the system operating conditions than observed in experimental testing. The convective and radiative contributions both continue to increase with row count. Considering these results along with the temperature results shows that the heat transfer coefficients increase with particle and tube temperatures.

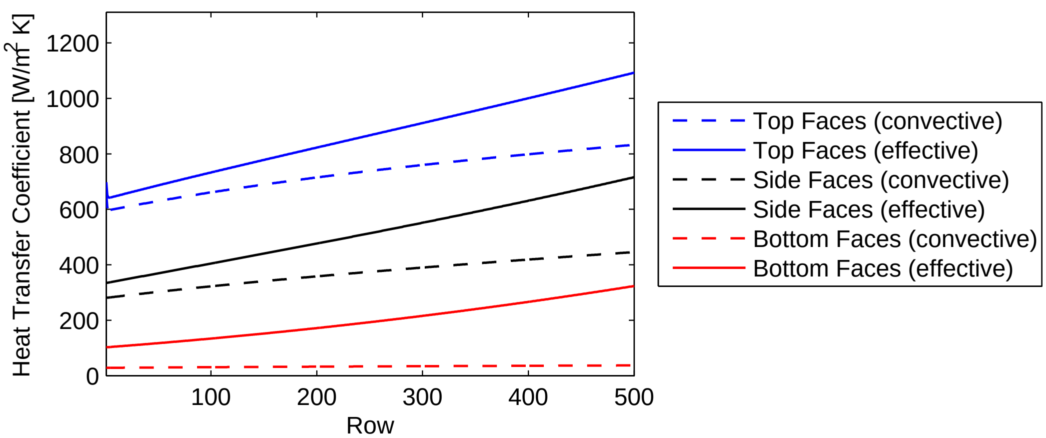

Figure 5.5: Average heat transfer coefficients per face by row

Energy flow within the tube array is visualized for select tubes near the top, middle and bottom of the receiver array in Figure 5.6. Here it can be seen that more of the energy going to the particles travels through the top and side tube faces. A portion of the energy input to the other nodes goes to the particles while the remainder goes towards the top surface through both conduction through the tube wall and reradiation internal to the tube. The variability between faces decreases down the height of the receiver as the heat transfer coefficients and the average tube temperatures increase. Radiation losses to the ambient are small and also increase with average tube temperature down the length of the receiver.

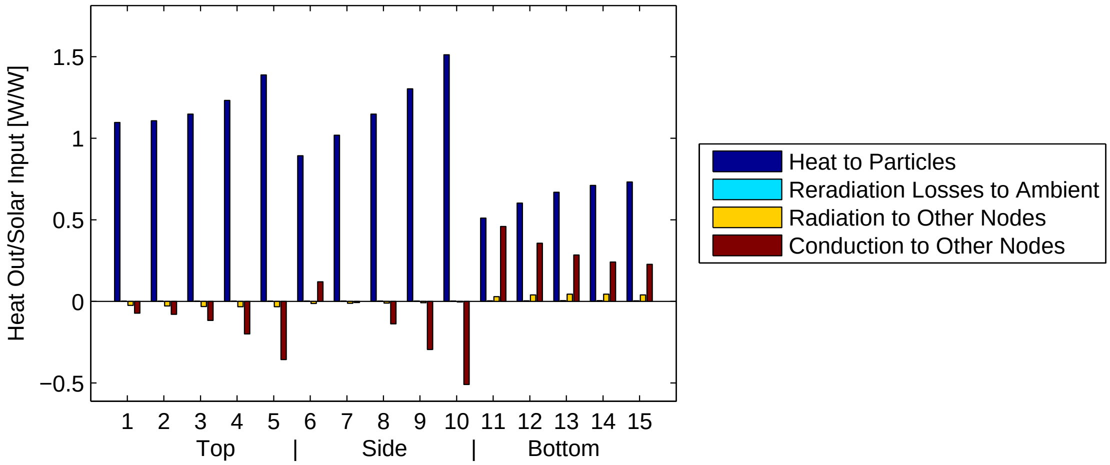

(a) Top Row

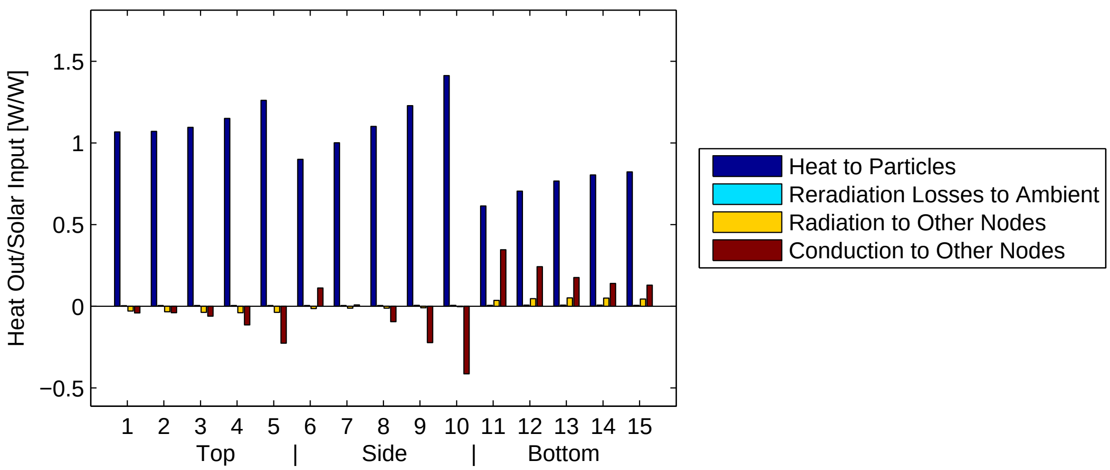

(b) Middle Row

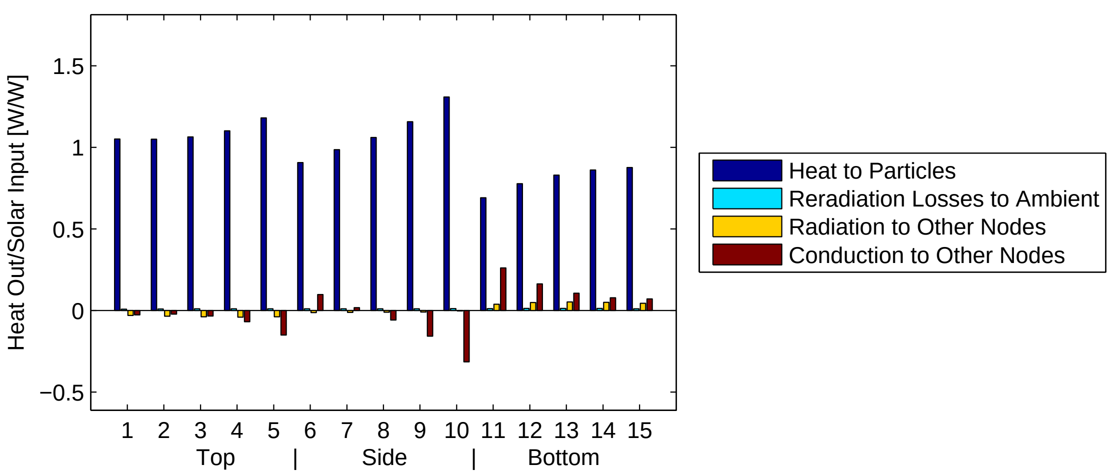

(c) Bottom Row

Figure 5.6: Normalized tube energy balances for each tube node

5.3 Full Receiver Simulation Discussion

Oscillations in the gas velocity are due to the varying height of the channels. The vertical channels are half the height of the inclined channels within the simulation, therefore, the cross-sectional area of the gas channel varies and the gas velocity alters to maintain a constant mass flow rate. This model does not include any recirculation that may occur in a functional 3D receiver. The cross-sectional area, and therefore gas velocity, are also affected by changes in the particle flow. Decreasing the depth or solids volume fraction also increases the effective gas channel area and forces the gas to slow down. The gas velocity, therefore, varies proportionately with the particle flow depth and solids volume fraction. This effect is more noticeable in the vertical channels where the changes are more substantial and the channel is narrower.

The average gas velocity increases with temperature due to expansion. Drag between this accelerating air and the particles then causes the average particle velocity to increase. Drag forces remain small relative to the other forces, however, so this increase is slight. As the average particle velocity increases it also causes the observed decreases in the average flow depth across the top surface and solids volume fraction within the vertical channels.

The observed convective heat transfer coefficients for the top and side faces are significantly higher primarily due to the increased bulk conductivity and thermal diffusivity of the particles at elevated temperatures. The bottom face convective HTC increases slightly due to increases in the gas phase conductivity and gas phase velocity that accompany temperature increases. Additionally, the radiative contribution is much greater due to the increased temperatures of the interacting surfaces. Continued heating down the length of the receiver continues to increase both the convective and radiative heat transfer due to further increased temperatures. These increases in the effective heat transfer coefficients cause the particle temperatures to approach the tube temperatures and also contribute to a decrease in the temperature distribution for each tube. Improved tube wall conductivity and increased reradiation on the solar side of the tube at higher temperatures also contribute to lower tube temperature discrepancies as heat can flow more easily between nodes and over smaller temperature differences.

Despite the increase in the effective HTC for all faces, the HTC for the top face remains 1.5 times higher than for the side face and 3 times higher than for the bottom face. This causes the net flow of heat from the bottom of each tube towards the top that is seen in the energy balances for each node. The amount of heat migrating between nodes decreases down the height of the receiver due to the increased effective heat transfer coefficients to the particles.

CHAPTER 6

SUMMARY & CONCLUSIONS

This research sought to more fully understand the heat transfer characteristics of the granular flow within NREL's Near-Blackbody Enclosed Particle Receiver, a concentrated solar power concept using hexagonal solar receiver tubes and solid particles as both the heat transfer fluid and the energy storage medium. This was done through both direct experimental measurement of the heat transfer coefficients from each face of a single tube and through the development of a simplified one-dimensional model.

Through low-temperature experimentation, it was discovered that the heat transfer coefficients are overall quite low for the desired application as shown in Table 6.1. In particular, the bottom face heat transfer coefficient is less than 30 W/m^2-K. Visualization of the particle flow showed that heat transfer coefficients correlate with particle contact. The top face has particle contact along the full length of the face and the highest HTC, the side face has intermittent and varied particle contact and a moderate HTC while the bottom face has little to no particle contact and a low HTC. Studies were also conducted to examine the average HTC for each of an array of 10 simulated absorber tubes and showed that the erratic nature of the particle flow can lead to a wide spread in values. Finally, studies also showed that increases in mass flow rate lead to overall increases in average heat transfer coefficients, and decreasing the particle diameter showed improved HTC values but at the expense of decreased maximum flow rates.

Table 6.1: Experimentally determined average heat transfer coefficients for each face at maximum particle flow conditions using 300 µm particles at 25°C

Tube Face	Average Effective Heat Transfer Coefficient
Top Face	303 W/m^2-K
Side Face	156 W/m^2-K
Bottom Face	23 W/m^2-K

In order to more fully understand these results, a model was developed using MATLAB to simulate heat transfer within the NBB design. Each face of the receiver was described by a unique heat transfer correlation. The top face was treated as an inclined plate with sufficient particle contact. For the side face, a correlation for plug flow through a vertical channel was modified by increasing the "effective" film thickness at the walls to account for the flow separation observed in experiments. The bottom face was modeled as a thin channel of air between the bottom tube surface and the upper surface of the granular flow. Entry length effects are significant over the short length of the face and were accounted for. The parameters needed for these correlations were calculated using a 1D channel model of the granular flow. Additionally, the solar side of the tube was included by assuming a constant input flux to each face and using 3D view factors to capture reradiation effects between tube nodes and to the ambient. The system was solved by incorporating an energy balance on the tubes, a mass balance on the gas phase and mass, momentum and energy equations for the particle flow.

Comparison with the experimental results for the 300 μm particle batch showed good agreement for all faces at maximum flow rates and captured the overall trends with changes in mass flow rate. The predicted HTC for the top face at the lowest mass flow rate was higher than that found in the experiments and a dip occurred in the side face HTC experimental results at the moderate mass flow rate that was not captured by the model. The model results also predicted the heat transfer results from the 200 μm particle batch for the top and bottom faces quite well when the simulation was run with 100 μm particles. This shows that the presence of increased fine particles in this particle batch had significant impact on the heat transfer characteristics. The side face heat transfer was not well predicted by the model. This is likely due to the oversimplification of using a constant "effective" film thickness.

The model developed was expanded to examine a full-sized NBB receiver by increasing the row count to 500. The results show that the convective and overall effective heat transfer coefficients are much improved at high temperatures as shown in Table 6.2. This is largely due to increases in thermal diffusivity and conductivity of the particle phase as temperatures increase. Additionally, radiation becomes a significant contributor and adds nearly 300 W/m^2-K to the HTC for each face. These increases in heat transfer also affect the flow of energy within each tube. Much of the incident solar flux is transferred towards the top tube surface by conduction and reradiation. The discrepancy between faces decreases as the overall average tube temperatures and heat transfer coefficients increase, which also leads to more uniform temperatures for each tube.

Table 6.2: Model predicted average heat transfer coefficients for each face at maximum particle flow conditions using 300 µm particles at 800°C

Tube Face	Average Effective Heat Transfer Coefficient
Top Face	1093 W/m^2-K
Side Face	716 W/m^2-K
Bottom Face	323 W/m^2-K

6.1 Future Work

The accuracy of the model shows confidence in this modeling technique. However, significant shortcomings do exist. Using a constant "effective" film thickness for the side wall heat transfer appears to be an oversimplification. Finding ways to correlate this value to the other flow conditions could improve its accuracy. Additionally, the solar side of the model is greatly simplified and likely not representative. Incorporating the heat transfer models into a more complex solar model that includes changes along the length of the tube could prove beneficial. This was beyond the scope of this project, however, and would likely hinder full receiver simulations.

Confidence in the model could be improved by high temperature validation. Future work could include expanded experimentation to allow for such a comparison. Additionally, the bed friction angle and solids volume fraction across the top face could be directly measured.

Despite these shortcomings, the model's dependency upon the physical dimensions and real parameters of the system offers the possibility of its use in design studies. Varying the parameters of the model such as the physical tube dimensions, particle properties and tube properties could shed light on important design improvements. The model could also be expanded to the system level to allow for system sizing and cycle analysis.

REFERENCES CITED

[1] Renewable resource data center. web. URL `http://rredc.nrel.gov/tidbits.html`.

[2] Manuel Romero and Jose Gonzalez-Aguilar. Solar thermal csp technology. *Wiley Interdisciplinary Reviews: Energy and Environment*, 3(1):42–59, 2014. ISSN 2041-840X. doi: 10.1002/wene.79. URL `http://dx.doi.org/10.1002/wene.79`.

[3] Craig S. Turchi, Zhiwen Ma, Ty Neises, and Michael Wagner. Thermodynamic Study of Advanced Supercritical Carbon Dioxide Power Cycles for High Performance Concentrating Solar Power Systems. In *Proceedings of ASME 2012 6th International Conference on Energy Sustainability*, 2012. doi: 10.1115/ES2012-91179.

[4] Paul Denholm and Marissa Hummon. Simulating the value of concentrating solar power with thermal energy storage in a production cost model. Technical Report NREL/TP-6A20-56731, National Renewable Energy Laboratory, November 2012.

[5] Antoni Gil, Marc Medrano, Ingrid Martorell, Ana Lzaro, Pablo Dolado, Beln Zalba, and Luisa F. Cabeza. State of the art on high temperature thermal energy storage for power generation. part 1concepts, materials and modellization. *Renewable and Sustainable Energy Reviews*, 14(1):31 – 55, 2010. ISSN 1364-0321. doi: http://dx.doi.org/10.1016/j.rser.2009.07.035. URL `http://www.sciencedirect.com/science/article/pii/S1364032109001774`.

[6] D. Laing, W. D. Steinmann, P. Veibahn, F. Grater, and C. Bahl. Economic analysis and life cycle assessment of concrete thermal energy storage for parabolic trough power plants. *Journal of Solar Energy Engineering*, 132(4), October 2010.

[7] Doerte Laing, Carsten Bahl, Thomas Bauer, Dorothea Lehmann, and Wolf-Dieter Steinmann. Thermal energy storage for direct steam generation. *Solar Energy*, 85(4):627 – 633, 2011. ISSN 0038-092X. doi: http://dx.doi.org/10.1016/j.solener.2010.08.015. URL `http://www.sciencedirect.com/science/article/pii/S0038092X10002835`. SolarPACES 2009.

[8] Zhiwen Ma, Greg C. Glatzmaier, and Mark Mehos. General development of solid particle thermal energy storage for concentrating solar power plants that use fluidized bed technology. In *Proceedings of ASME 2013 7th International Conference on Energy Sustainability & 11th Fuel Cell Science, Engineering and Technology Conference*, 2013.

[9] Zhiwen Ma, Greg Glatzmaier, and Mark Mehos. Fluidized Bed Technology for Concentrating Solar Power With Thermal Energy Storage. *Journal of Solar Energy Engineering-Transactions of the ASME*, 136(3), AUG 2014. ISSN 0199-6231. doi: {10.1115/1.4027262}.

[10] J. Martin and J. Vitko. Ascuas: A solar central receiver utilizing a solid thermal carrier. Technical Report SAND82-8203, Sandia National Laboratories, 1982.

[11] P. K. Falcone, J. E. Noring, and J. M. Hruby. Assessment of a solid particle receiver for a high temperature solar central receiver system. Technical Report SAND85-8208, Sandia National Laboratories, 1985.

[12] J. M. Hruby. A technical feasibility study of a solid particle solar central receiver for high temperature applications. Technical Report SAND86-8211, Sandia National Laboratories, 1986.

[13] J. Hruby, R. Steeper, G. Evans, and C. Crowe. An experimental and numerical study of flow and convective heat transfer in a freely falling curtain of particles. *Journal of Fluids Engineering*, 110(2), 1988. doi: 10.1115/1.3243531.

[14] Nathan P. Siegel, Clifford K. Ho, Siri S. Khalsa, and Gregory J. Kolb. Development and evaluation of a prototype solid particle receiver: On-sun testing and model validation. *Journal of Solar Energy Engineering*, 132(2), 2010. doi: 10.1115/1.4001146.

[15] Marc Roger, Lars Amsbeck, Birgit Gobereit, and Reiner Buck. Face-down solid particle receiver using recirculation. *Journal of Solar Energy Engineering*, 133, August 2011.

[16] Gang Xiao, Kaikai Guo, Zhongyang Luo, Mingjiang Ni, Yanmei Zhang, and Cheng Wang. Simulation and experimental study on a spiral solid particle solar receiver. *Applied Energy*, 113(0):178 – 188, 2014. ISSN 0306-2619. doi: http://dx.doi.org/10.1016/j.apenergy.2013.06.045. URL `http://www.sciencedirect.com/science/article/pii/S0306261913005527`.

[17] M. J. Rightley, L. K. Matthews, and G. P. Mulholland. Experimental characterization of the heat transfer in a free-falling-particle receiver. *Solar Energy*, 48(6):363–374, 1992.

[18] Janna Martinek and Zhiwen Ma. Granular Flow and Heat Transfer Study in a Near-Blackbody Enclosed Particle Receiver. In *ASME 2014 8th International Conference on Energy Sustainability collocated with the ASME 2014 12th International Conference on Fuel Cell Science, Engineering and Technology*, volume 1, 2014. doi: 10.1115/ES2014-6393.

[19] Zhiwen Ma. Methods and systems for concentrated solar power, 2013.

[20] JC Chen, JR Grace, and MR Golriz. Heat transfer in fluidized beds: design methods. *Powder Technology*, 150(2):123–132, FEB 16 2005. ISSN 0032-5910. doi: {10.1016/j.powtec.2004.11.035}.

[21] VA Borodulya, YS Teplitsky, II Markevich, AF Hassan, and TP Yeryomenko. Heat-transfer between a surface and a fluidized-bed-considerations of pressure and temperature. *International Journal of Heat and Mass Transfer*, 34(1):47–53, JAN 1991. ISSN 0017-9310. doi: {10.1016/0017-9310(91)90171-A}.

[22] H A Vreedenberg. Heat transfer between a fluidized bed and a vertical tube. *Chemical engineering science*, 11(4):274 – &, 1960.

[23] H A Vreedenberg. Heat transfer between a fluidized bed and a horizontal tube. *Chemical engineering science*, 9(1):52 – 60, 1958.

[24] H. S. Mickley and D. F. Fairbanks. Mechanism of heat transfer to fluidized beds. *AIChE Journal*, 1(3):374–384, 1955. ISSN 1547-5905. doi: 10.1002/aic.690010317. URL `http://dx.doi.org/10.1002/aic.690010317`.

[25] Hiromi Takeuchi. Particles flow pattern and local heat transfer around tube in moving bed. *AIChE Journal*, 42(6):1621–1626, 1996. ISSN 1547-5905. doi: 10.1002/aic.690420613. URL `http://dx.doi.org/10.1002/aic.690420613`.

[26] J. Niegsch, D. Kneke, and P.-M. Weinspach. Heat transfer and flow of bulk solids in a moving bed. *Chemical Engineering and Processing: Process Intensification*, 33(2):73 – 89, 1994. ISSN 0255-2701. doi: http://dx.doi.org/10.1016/0255-2701(94)85006-2. URL `http://www.sciencedirect.com/science/article/pii/0255270194850062`.

[27] Hany Al-Ansary, Abdelrahman El-Leathy, Zeyad Al-Suhaibani, Sheldon Jeter, Dennis Sadowski, Abdulaziz Alrished, and Matthew Golob. Experimental study of a sand-air heat exchanger for use with a high-temperature solar gas turbine system. *Journal of Solar Energy Engineering*, 134(4), October 2012.

[28] W.N. Sullivan and R.H. Sabersky. Heat transfer to flowing granular media. *International Journal of Heat and Mass Transfer*, 18(1):97 – 107, 1975. ISSN 0017-9310. doi: http://dx.doi.org/10.1016/0017-9310(75)90012-5. URL `http://www.sciencedirect.com/science/article/pii/0017931075900125`.

[29] JK Spelt, CE Brennen, and RH Sabersky. Heat-transfer to flowing granular material. *International Journal of Heat and Mass Transfer*, 25(6):791–796, 1982. ISSN 0017-9310. doi: {10.1016/0017-9310(82)90091-6}.

[30] J.S. Patton, R.H. Sabersky, and C.E. Brennen. Convective heat transfer to rapidly flowing, granular materials. *International Journal of Heat and Mass Transfer*, 29(8):1263 – 1269, 1986. ISSN 0017-9310. doi: http://dx.doi.org/10.1016/0017-9310(86)90159-6. URL `http://www.sciencedirect.com/science/article/pii/0017931086901596`.

[31] Matthew Golob, Sheldon Jeter, and Dennis Sadowski. Heat transfer coefficient between flat surface and sand. In *Proceedings of the ASME 5th International Conference on Energy Sustainability 2011, PTS A-C*, pages 1441–1450, 2012. ISBN 978-0-7918-5468-6.

[32] VVR Natarajan and ML Hunt. Heat transfer in vertical granular flows. *Experimental Heat Transfer*, 10(2):89–107, APR-JUN 1997. ISSN 0891-6152.

[33] VVR Natarajan and ML Hunt. Kinetic theory analysis of heat transfer in granular flows. *International Journal of Heat and Mass Transfer*, 41(13):1929–1944, JUL 1998. ISSN 0017-9310. doi: {10.1016/S0017-9310(97)00315-3}.

[34] K.S. Rajan, K. Dhasandhan, S.N. Srivastava, and B. Pitchumani. Studies on gas-solid heat transfer during pneumatic conveying. *International Journal of Heat and Mass Transfer*, 51(1112):2801 – 2813, 2008. ISSN 0017-9310. doi: http://dx.doi.org/10.1016/j.ijheatmasstransfer.2007.09.042. URL `http://www.sciencedirect.com/science/article/pii/S0017931007006424`.

[35] J. Bandrowski and G. Kaczmarzyk. Gas-to-particle heat transfer in vertical pneumatic conveying of granular materials. *Chemical Engineering Science*, 33(10):1303 – 1310, 1978. ISSN 0009-2509. doi: http://dx.doi.org/10.1016/0009-2509(78)85111-2. URL `http://www.sciencedirect.com/science/article/pii/0009250978851112`.

[36] J Guderian, D Kneke, and P.-M Weinspach. Heat transfer to trickling granular materials. *Chemical Engineering and Processing: Process Intensification*, 30(3):157 – 174, 1991. ISSN 0255-2701. doi: http://dx.doi.org/10.1016/0255-2701(91)85005-9. URL `http://www.sciencedirect.com/science/article/pii/0255270191850059`.

[37] Yoel Forterre and Olivier Pouliquen. Flows of dense granular media. *Fluid Mechanics*, 40:1–24, January 2008.

[38] GDR Midi. On dense granular flows. *The European Physical Journal E*, 14(4):341–365, 2004. ISSN 1292-8941. doi: 10.1140/epje/i2003-10153-0. URL `http://dx.doi.org/10.1140/epje/i2003-10153-0`.

[39] Michel Y. Louge and Stephen C. Keast. On dense granular flows down flat frictional inclines. *Physics of Fluids (1994-present)*, 13(5):1213–1233, 2001. doi: http://dx.doi.org/10.1063/1.1358870. URL `http://scitation.aip.org/content/aip/journal/pof2/13/5/10.1063/1.1358870`.

[40] R. Delannay, M. Louge, P. Richard, N. Taberlet, and A. Valance. Towards a theoretical picture of dense granular flows down inclines. *Nature Materials*, 6:99–108, February 2007.

[41] Birte Domnik and Shiva P. Pudasaini. Full two-dimensional rapid chute flows of simple viscoplastic granular materials with a pressure-dependent dynamic slip-velocity and their numerical simulations. *Journal of Non-Newtonian Fluid Mechanics*, 173:72–86, APR 2012. ISSN 0377-0257. doi: {10.1016/j.jnnfm.2012.03.001}.

[42] Birte Domnik, Shiva P. Pudasaini, Rolf Katzenbach, and Stephen A. Miller. Coupling of full two-dimensional and depth-averaged models for granular flows. *Journal of Non-Newtonian Fluid Mechanics*, 201:56–68, NOV 2013. ISSN 0377-0257. doi: {10.1016/j.jnnfm.2013.07.005}.

[43] Colin Bailey. Stainless steel thermal properties. URL `http://www.mace.manchester.ac.uk/project/research/structures/strucfire/materialInFire/Steel/StainlessSteel/thermalProperties.htm`.

[44] John R. Howell. A catalog of radiation heat transfer configuration factors. web. URL `http://www.thermalradiation.net/indexCat.html`.

[45] Theodore L. Bergman, Adrienne S. Lavine, Frank P. Incropera, and David P. Dewitt. *Fundamentals of heat and Mass Transfer*. John Wiley & Sons, 2011.

[46] R. K. Shah and A. L. London. *Laminar Flow Forced Convection in Ducts*. Advances in Heat Transfer. Academic Press, 1978.

[47] Andrew Oles. *Modeling of Solar Particle Receivers for Hydrogen Production and Thermochemical Energy Storage*. PhD thesis, University of Maryland, 2014.

[48] G Malherbe, J-F Henry, A El Bakali, C Bissieux, and S Fohanno. Measurement of thermal conductivity of granular materials over a wide range of temperatures. comparison with theoretical models. *Journal of Physics: Conference Series*, 395(1):012081, 2012. URL `http://stacks.iop.org/1742-6596/395/i=1/a=012081`.

[49] Clayton Crowe, Martin Sommerfeld, and Yutaka Tsuji. *Multiphase Flows with Droplets and Particles*. CRC Press, 1998.

[50] Kevin Albrecht. Multiphase, multi-component, chemically reacting, counter-current, channel flow using a eulerian approach. August 2014.

[51] Ihsan Barin. *Thermochemical Data of Pure Substances*. Weinheim, 2nd edition, 1993.